Simulation of the filling process during the Resin Transfer Molding

[FEIFEI ZHAO]

A thesis submitted to the faculty of
Ecole Centrale de Nantes
Erasmus Mundus program

Master of Computational Mechanics

[Steven Le Corre], Professor

Department of Compational Mechanics

Ecole Cenrale de Nantes

[June] [2011]

ABSTRACT

Simulation of the filling process during the Resin Transfer Molding

[FEIFEI ZHAO]

Department of Computational Mechanics

Master of Computational Mechanics

Since the spread of the large amount use of the resin, tremendous interests have been put to use it to mold different kinds of materials. Because of this reason, tons of researches have been done for this molding process both experimentally and numerically. The aim of this thesis was to perform a numerical simulation of the mold filling process during resin transfer molding(RTM) using the finite element method(FEM). As sometimes the cavity used for the molding is porous media. the Darcy's law for the porous media was employed along with the incompressible assumption to construct the governing differential equation. Before the simulation, the specific description of the derivation of the finite element method for the PDE was done.

All the results are checked with the commercial software COMSOL. The proposed model is a square domain with porous media inside. Several tests have been done for the simulation. The first test was done for a homogeneous mesh with the coefficient of the Brinkman term to be zero which make the equation degrade to be the Stokes equation. The results were compared between the Brinkman and Stokes systems. Then the capillary pressure was tested. The 3D test and finer mesh were also studied within the thesis. After the domain was changed to be consisted with three layers of different materials, the same tests were carried out for the half of the symmetrical mold. And the anisotropic permeability was imposed, the influence of the angle of the anisotropic was also studied. Finally, by using level set method, the propagation of the flow front during the filling process was researched.

After all the simulations described above, conclusions were done together with the illustration of the problems occurred during the thesis and a simple preview of the work.

Keywords: Resin Transfer Molding(RTM), finite element, Newton Raphson

ACKNOWLEDGMENTS

This dissertation would not have been possible without the guidance and the help of several individuals who in one way or another contributed and extended their valuable assistance in the preparation and completion of this study.

First and foremost, my utmost gratitude to Dr. Steven Le Corre, my supervisor in Ecole Centrale de Nantes whose sincerity and encouragement I will never forget. Dr. Steven has been my inspiration as I hurdle all the obstacles in the completion this research work.

Giraldo Arias Santiago, the master from Columbia, for his patience and steadfast encouragement to complete this study;

Fabien Poulhaon, the master from France, for the moral support despite his just being newly appointed and his help during the two years of France;

Shabeer Khan, the master from Pakistan, for his frequently asking of everything, from which I learned a lot including language and the culture of Pakistan;

Lian Weidong, the excellent phD from China, for his patience in explaining the use of the Xfem library and the help in the coding which is really valuable for me;

Last but not the least, my family and the one above all of us, the omnipresent God, for answering my prayers for giving me the strength to plod on despite my constitution wanting to give up and throw in the towel, thank you so much Dear Lord.

Contents

List of Figures

Chapter 1

Introduction

1.1 Resin transfer molding

The resin transfer molding(RTM) is one of most popular manufacturing processes of composite structures. RTM is a technique of liquid composite molding(LCM) wherein a thermosetting resin is injected into a closed mold into which a fiber preform has been placed. The fiber preform(typically composed of fiberglass, carbon or graphite) imparts tensile strength, stiffness, toughness and mechanical reinforcement to the part. The thermosetting resins(typically epoxy, polyamides, polyesters and phenolic) help in binding the fiber together, and impart compressive strength, dimensional and thermal stability and good fatigue properties to the part.

The RTM is used to produce medium/large parts with two smooth surfaces in an efficient way because the resin is injected into mold after fiber perform is installed in mold [1]. Figure 1.1 describes the typical molding process. After placing the reinforcement perform between mold and counter-mold, the mold is closed and the resin is injected under low pressure, thus wetting the fibers.

RTM is gaining popularity because of its net-shape forming capability, easy tailoring of final

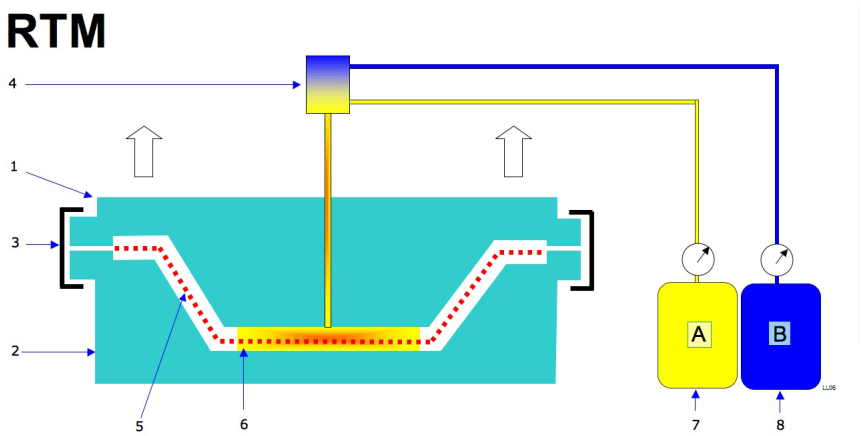

Figure 1.1 The Scheme of Resin Transfer Molding Process

part properties, ease of use, and lower molding costs and time relative to other techniques like hand-layup and filament winding. RTM has been used to manufacture ship hulls, wheels bases for armored vehicles, and freight car panels, and numerous parts on military aircraft. Figure 1.2 shows some applications of RTM.

(a) the auto panel (b) the hull (c) the wind turbine

Figure 1.2 some applications of RTM

The control of RTM is essentially a disturbance rejection problem in a batch setting. The main objective of RTM is to successfully fill a given mold without any dry spots [2].

RTM process involves many process parameters such as injection pressure, temperature of the mold, permeability of the fiber mat, resin viscosity, location of gates and vents. In order to achieve a high-quality composite parts free of dry spots with minimum impregnation cycle time, it is very important to optimize these process parameters. Traditional experimental methods for the optimization of mold and process design are time consuming and economically prohibitive so that computer based simulation of the process can help manufacturers optimize various parameters involved before piratical production [3]. A model capable of predict resin flow behavior and pressure gradients inside the mold can be used to optimize the process parameters of RTM.

1.2 Finite element method, Xfem library and Level Set method

Several methods have been used to simulate the RTM process. In this paper, the finite element method was employed.

The modern development of the finite element method began in the 1940s in the field of structural engineering with the work by Hrennikoff in 1941 and McHenry in 1943, who used a lattice of line (one-dimensional) elements (bars and beams) for the solution of stresses in continuous solids. In a paper published in 1943 but not widely recognized for many years, Courant proposed setting up the solution of stresses in a variational form. Then he introduced piecewise interpolation (or shape) functions over triangular subregions making up the whole region as a method to obtain approximate numerical solutions. In 1947 Levy developed the flexibility or force method, and in 1953 his work suggested that another method (the stiffness or displacement method) could be a promising alternative of use in analyzing

statically redundant aircraft structures. However, his equations were cumbersome to solve by hand, and thus the method became popular only with the advent of the high-speed digital computer.

In 1954 Argyris and Kelsey developed matrix structural analysis methods using energy principles. This development illustrated the important role that energy principles would play in the finite element method. The first treatment of two-dimensional elements was by Turner et al. in 1956. They derived stiffness matrices for truss elements, beam elements, and two-dimensional triangular and rectangular elements in plane stress and outlined the procedure commonly known as the direct stiffness method for obtaining the total structure stiffness matrix. Along with the development of the high-speed digital computer in the early 1950s, the work of Turner et al.prompted further development of FE stiffness equations expressed in matrix notation. The phrase FE was introduced by Clough in 1960 when both triangular and rectangular elements were used for plane stress analysis.

From the early 1950s to the present, enormous advances have been made in the application of the FEM to solve complicated engineering problems Engineers, applied mathematicians, and other scientists will undoubtedly continue to develop new applications [4].

In spite of its decades of existence, the FEM coupled with meshing tools does not yet manage to simulate efficiently the propagation of 3D cracks for geometries relevant to engineers in industry. This fact was the motivation behind the design of the eXtended Finite Element Method(X-FEM) [5].

The institute GeM in Ecole Centrale de Nantes develop the library of classes and functions

of C++ based on the XFEM. It allows the application to implement the calculations based on the approach. The library uses the objects programming and the generic programming (templates) of C++. It is not strictly customized for some kinds of problem, but it could be the toolbox for the further development. A number of applications could be found in the Applis directory [6].

The level set method (sometimes abbreviated as LSM) is a numerical technique for tracking interfaces and shapes. The advantage of the level set method is that one can perform numerical computations involving curves and surfaces on a fixed Cartesian grid without having to parameterize these objects (this is called the Eulerian approach) [7]. Also, the level set method makes it very easy to follow shapes that change topology, for example when a shape splits in two, develops holes, or the reverse of these operations. All these make the level set method a great tool for modeling time-varying objects, like inflation of an airbag, or a drop of oil floating in water [8].

During the work, the level set was used for two aspects. The first one is to distinguish the materials. As level set method is powerful to follow the track of the shape, thus if there are some layers of materials, it could be convenient to employ LSM. The second aspect is as the motivation for the level set method to be invented, to propagate the flow front. In this case, flow front would be a level set and the propagation of the flow front could be studied.

1.3 Gmsh and COMSOL

The Xfem library uses gmsh to import the mesh and export their result. Gmsh is a 3D finite element grid generator with a build-in CAD engine and post-processor. Its design goal is to provide a fast, light and user-friendly meshing tool with parametric input and advanced

visualization capabilities. Gmsh is built around four modules: geometry, mesh, solver and post-processing. The specification of any input to these modules is done either interactively using the graphical user interface or in ASCII text files using Gmsh's own scripting language. Gmsh is copyright (C) 1997-2011 by C. Geuzaine and J.-F. Remacle and is distributed under the terms of the GNU General Public License (GPL) (Version 2 or later, with an exception to allow for easier linking with external libraries). In short, this means that everyone is free to use Gmsh and to redistribute it on a free basis. As it is an open source software and provides the interface to export the files, it is convenient to use it to check the result [9].

The software COMSOL was used to verify the result of the simulation. The first name of COMSOL was Toolbox because it solved PDEs. Then the second name was made to be FEMLAB as it was based on the Finite Element Method. And now it is called Multiphysics and it deals withe multi-physics problem. Comsol Multiphysics is an integrated environment for solving systems of time-dependent or stationary second order in space partial differential equations in one, two, and three dimensions. Moreover, such equations may be coupled in an almost arbitrary way. Comsol Multiphysics provides sophisticated (and convenient) tools for geometric modeling. Therefore, for many standard problems, there exist predened so-called application modes which act like templates in order to hide much of the complex details of modeling by equations. The application modes make use of the language used in the respective engineering discipline [10].Figure 1.3 are some applications of Comsol in real industry.

Thus Comsol is a good choice to check the result as it also uses finite element method and it solves the CFD problems very well.

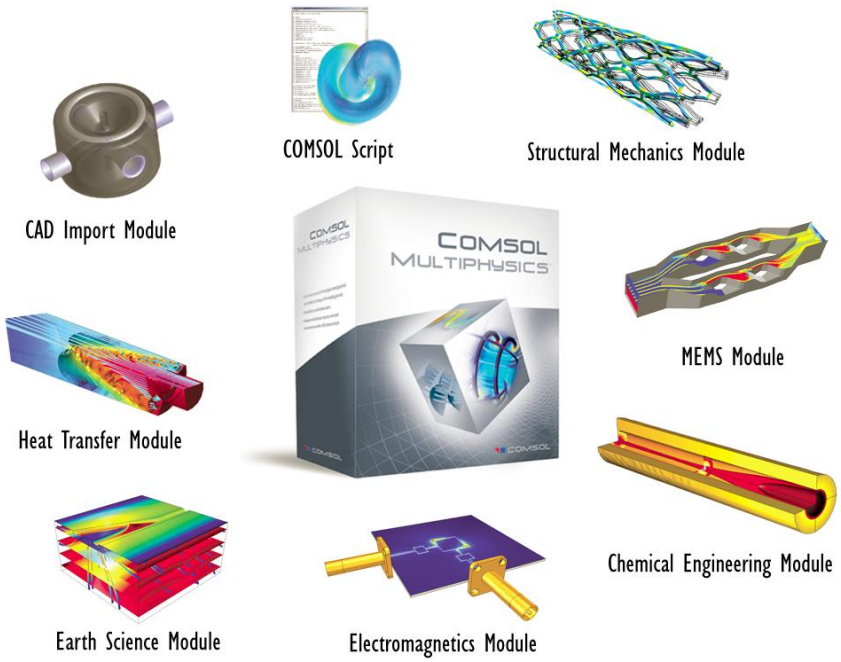

Figure 1.3 Some applications of Comsol in real industry

1.4 RTM simulation: a short review

Because mold cost increases with part complexity, numerical simulation of RTM process is becoming more and more important. A simulation for filling stage in RTM will reduce the time required to design a mold and also assure the quality of the products. Several researchers have published about the numerical modeling. Bruschke and Advani (1990) developed a 2-dimensional numerical scheme, and Young and et al. (1991) developed 2 and 3-dimensional schemes by control volume finite element method (CVFEM) for the filling stage. Chan and Hwang (1998) developed 2-dimensional numerical model by least squares FEM, Wu and Hourng (1995) simulated filling process in order to explain the phenomena of edge effects by the boundary fitted FEM, and Yoo (1996) developed 2-dimensional model by the boundary element method. Phelam Jr. (1997) simulated filling using 2 and 3-dimensional FEM and flow analysis network.

An important interest in RTM process is to minimize cycle time without sacrificing part quality and increasing cost. There are a lot of processing variables in RTM process, and one of the most critical factors is to determine gate location, which is especially important in complex mold geometries. Determining gate locations by trial and error is not practical because the retooling is expensive and time inefficient, which was mentioned in prior work by Pandelidis and Zou (1990), Noller (1991) and Catoen (1993). A numerical simulation to predict these variables can provide a design tool, once the locations of inlet gates has been specified. There are so many possible choices for gate locations as node numbers in the finite element mesh for the mold geometry, however. In addition to that, the filling time with respect to the location of gates is non-linear, hence there is a need for developing systematic search method which can be interactively coupled with filling simulation capabilities to determine optimum gate locations. The genetic algorithm (GA) as a searching method, which was proposed by Goldberg (1989), was used for this study. GA was applied to search method by Caroll (1996) for dealing with highly nonlinear and large spaces having many possible local optima. An optimization study of finding gate and vent locations using GA was performed by Mathur and et al. (1999) in case of simple 2-dimensional geometry.

Another important variable in process design is the injection pressure. The injection pressure directly affects the industrial costs. The use of multiple port injection can greatly speed up mold filling for large part without increasing injection pressure. Though the simultaneous multiple injection process can dramatically reduce fill time, the process has the potential of containing much void contents where two or more flow fronts meet. The sequential injection process, proposed by Chan (1992), was used in this study to minimize cycle time without sacrificing part quality nor increasing cost [11].

Chapter 2

Model and Numerical Methods

2.1 Brinkman Formulation

In order to simulate the filling process, several assumptions must be made to simplify the problem. In the present study,the preplaced fiber mat in the mold cavity are assumed to be rigid, and no deformation occur during mold filling. Interia effects are neglected because of the high viscosity which leads to the low Reynolds number of the resin flow. Furthermore, surface tension is considered negligible, as compared with the dominant viscous force [12]. The flow is thought to be incompressible, it should satisfy

$$div\,\overrightarrow{v} = 0 \tag{2.1}$$

where $\overrightarrow{v}$ is the velocity of the flow.

Using the standard assumptions, for the incompressible fluid , the total stress tensor is written as

$$\boldsymbol{T} = \boldsymbol{\sigma^d} - p\boldsymbol{I} \tag{2.2}$$

Where p is the pressure and $\boldsymbol{\sigma^d}$ is the deviatoric stress, related the strain rate $\nabla^s \overrightarrow{v}$ by

$$\boldsymbol{\sigma^d} = 2\mu\nabla^s \overrightarrow{v} \tag{2.3}$$

where μ denotes the viscosity of the fluid. With such assumptions, the equilibrium is written in the form of an usual Stokes problem:

$$div\boldsymbol{\sigma^d} - \nabla p = 0 \tag{2.4}$$

However, the RTM process can not be modeled by the Stokes equation, as the medium is not as simple as the medium for previous case. Generally, the material during the RTM process is porous. Figure 2.1 shows the porous media material. The permeability k is used

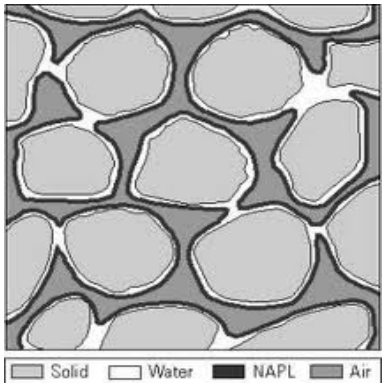

Figure 2.1 The Porous Media Material

to describe the homogenized behavior of the "porous" medium which in the scope of a full detailed simulation would lead to billions of degrees of freedom to the system, it becomes to be impossible to solve the Stokes equation with finite element method with the current CPU. Nevertheless the size of the cavity can be assumed much bigger than that of the pore size that the Darcy's law can be used to describe the flow inside the porous domain.

Darcy's law is a phenomenologically derived constitutive equation that describes the flow of a fluid through a porous medium. The law was formulated by Henry Darcy based on the results of experiments on the flow of water through beds of sand. It is a simple proportional relationship between the instantaneous flow rate through a porous medium, the viscosity of the fluid and the pressure drop over a given distance which as summarized by equation (2.5).

$$Q = \frac{-kA}{\mu}\frac{(P_b - P_a)}{L} \tag{2.5}$$

The total discharge, Q is equal to the product of the permeability of the medium, k, the cross sectional area to flow, A and the pressure drop, all divided by the viscosity, μ and the length the pressure drop is taking place over. The negative sign is needed because fluids flows from high pressure to low pressure.

Whereas Darcy's law assumes that velocity is proportional to the pressure gradient for a particular porous medium, Brinkman noted that, in general, the viscous effects must also be taken into account to model flow accurately through porous media. Heuristic generalizations of Darcy's law have been considered to model non-Darcy flows in porous media. Along with heuristic developments, theoretical justifications exist for the Brinkman model as an asymptotic approximation to the NSE, and references therein. Straughan [13] presents several of the most popular non-Darcy models for flow in porous media .

The Brinkman model, as described with equation (2.6), has been applied to approximate non-Darcian flows in a variety of contexts; e.g. it is used to model oil filtration flows, groundwater ows, forced convective flows in metal foam-filled pipes (used in the cooling of electronic equipment), gas diffusion through fuel cell membranes, Casson fluid flow in porous media (e.g. blood flow in vessels obstructed by fatty plaques and clots), and interstitial fluid flow through muscle cells with good accuracy. Brinkman equation is also used to model

turbulence in porous media in the macroscopic scales (for a discussion concerning turbulence modeling at the macroscopic versus the microscopic pore level) [13].

$$div\boldsymbol{\sigma^d} - \nabla p - c\,\overrightarrow{v} = 0 \tag{2.6}$$

The constant $c = \frac{\mu_e}{k}$, where μ_e is the dynamic viscosity with the unit of $Pa \cdot s$, k is the permeability of the material with the unit of m^2 This constant, generated by the property of the porous medium, is called drag coefficient. Therefore, the equation (2.4) is obtained as the governing equation for the Stokes system while the equation (2.6) is gained as the governing equation for the Brinkman system. Both systems are under the assumption of incompressible flow of equation (2.1).

2.2 Weak Form

To get the numerical scheme of the system, the finite element method was employed. The first step is to get the weak formulation of all the governing equations. For equation (2.4), the test function $\overrightarrow{v}^*$ was imposed. Equation (2.7) is the result of the integration of multi-production of equation (2.4) and the test function.

$$\forall \overrightarrow{v}^* : \quad \int_\Omega (div\boldsymbol{\sigma^d} \cdot \overrightarrow{v}^* - \nabla p \cdot \overrightarrow{v}^*) d\Omega = 0 \tag{2.7}$$

Using the divergence theorem for equation (2.7)

$$\forall \overrightarrow{v}^* : \quad \int_\Omega div(\boldsymbol{\sigma^d} \cdot \overrightarrow{v}^*) d\Omega = \int_{\partial\Omega} \boldsymbol{\sigma^d} \cdot \overrightarrow{n} \cdot \overrightarrow{v}^* d\partial\Omega = \int_\Omega div\boldsymbol{\sigma^d} \cdot \overrightarrow{v}^* d\Omega + \int_\Omega \boldsymbol{\sigma^d} : \nabla \overrightarrow{v}^* d\Omega \tag{2.8}$$

Similarly the second term of equation (2.7) can be calculated as

$$\forall \overrightarrow{v}^* : \quad \int_\Omega div(p \cdot \overrightarrow{v}^*) d\Omega = \int_{\partial\Omega} p\,\overrightarrow{v}^* \cdot \overrightarrow{n}\, d\partial\Omega = \int_\Omega \nabla p \cdot \overrightarrow{v}^* d\Omega + \int_\Omega p \nabla \overrightarrow{v}^* d\Omega \tag{2.9}$$

Thus the equation (2.7) could be rewritten as equation (2.10)

$$\forall \overrightarrow{v}^* : \quad -\int_\Omega (\boldsymbol{\sigma^d} : \nabla \overrightarrow{v}^* - p \cdot \nabla \overrightarrow{v}^*) d\Omega + \int_{\partial\Omega} (\boldsymbol{\sigma^d} \cdot \overrightarrow{n} \cdot \overrightarrow{v}^* - p\overrightarrow{n} \cdot \overrightarrow{v}^*) d\partial\Omega = 0 \tag{2.10}$$

By noticing equation (2.2) and $\overrightarrow{t} = \boldsymbol{T} \cdot \overrightarrow{n}$, equation (2.10) can be simplified to equation (2.11)

$$\forall \overrightarrow{v}^* : \ -\int_\Omega (\boldsymbol{\sigma^d} : \nabla \overrightarrow{v}^* - p \cdot \nabla \overrightarrow{v}^*) d\Omega + \int_{\partial\Omega} (\overrightarrow{t} \cdot \overrightarrow{v}^*) d\partial\Omega = 0 \tag{2.11}$$

For the mass conservation, the test function of pressure p^* was imposed. And the corresponding weak formulation is equation (2.12)

$$\forall p^* : \ -\int_\Omega (p^* \cdot div\, \overrightarrow{v}) d\Omega = 0 \tag{2.12}$$

As the incompressibility condition should be satisfied in all the domains, the Stokes equation and the mass conservation must be mixed to be solved. Plus equation (2.11) and (2.12) and by noticing $\boldsymbol{\sigma^d} - p\boldsymbol{I} = \boldsymbol{T}$, the mixed formulation can be written as,

$$\forall (\overrightarrow{v}^*, p^*) : \ \int_\Omega \boldsymbol{T} : \nabla \overrightarrow{v}^* d\Omega - \int_{\partial\Omega} (\overrightarrow{t} \cdot \overrightarrow{v}^*) d\partial\Omega - \int_\Omega (p^* \cdot div\, \overrightarrow{v}) d\Omega = 0 \tag{2.13}$$

Similarly, to solve the system in the domain of porous medium, the equation (2.1) and (2.6) have to be mixed. Imposing the test function of pressure p^* for the equation (2.1) and the test function of $\overrightarrow{v}^*$ for the equation (2.6), the weak formulation can be written as,

$$\forall (\overrightarrow{v}^*, p^*) : \ \int_\Omega (div \boldsymbol{\sigma^d} - \nabla p - c\overrightarrow{v}) \cdot \overrightarrow{v}^* d\Omega - \int_\Omega p^* div\, \overrightarrow{v} = 0 \tag{2.14}$$

By using the divergence theorem for the first and the second term of the first integration, the weak formulation can be rewritten as,

$$\forall (\overrightarrow{v}^*, p^*) : \ \int_\Omega \boldsymbol{T} : \nabla \overrightarrow{v}^* d\Omega - \int_{\partial\Omega} (\overrightarrow{t} \cdot \overrightarrow{v}^*) d\partial\Omega - \int_\Omega (p^* \cdot div\, \overrightarrow{v}) d\Omega + \int_\Omega c\overrightarrow{v} \cdot \overrightarrow{v}^* d\Omega = 0 \tag{2.15}$$

Up to now, the weak formulation for both the Stokes system and the porous medium system has been obtained as equation (2.13) and (2.15) respectively. The $\overrightarrow{v}^*$ and p^* are the test function for velocity and pressure respectively.

2.3 Newton Raphson method

Numerically, all the problems have to be solved discretized. Thus the first step to solve the problem is to discretize the equations and then solve the value for the variables at the discretized nodes. With finite element, the shape function is usually used to discretize the equations.

Starting from the weak formulation (2.13) for Stokes system and (2.15) for the Brinkman system, as $\overrightarrow{v}$ and p are the variables to be solved but not the test function $\overrightarrow{v}^*$ and p^*, the first step is to discretize the test function. By introducing $[N_v]$ to be the shape function of the velocity and $[N_p]$ to be the shape function of the pressure, the test function $\overrightarrow{v}^*$ should be $\overrightarrow{v}^* = \{\overrightarrow{v}^*_{node}\}[N_v]$, and the test function p^* could be $p^* = \{p^*_{node}\}[N_p]$. Where $\{\overrightarrow{v}^*_{node}\}$ and $\{p^*_{node}\}$ are the values at the node for test velocity and test pressure respectively.

By comparing the equation (2.13) for the Stokes system and the equation (2.15), the only difference occurred is the last term, the term with the drag coefficient. Thus for the algorithm description below, only the Brinkman were taken. Using the interpolation for the test function of $\overrightarrow{v}^*$ and p^*, the Brinkman equation (2.15) could be rewritten as,

$$\begin{aligned}\forall(\overrightarrow{v}^*, p^*): \quad & \int_\Omega \boldsymbol{T} : \{\{\overrightarrow{v}^*_{node}\}\nabla[N_v]\}d\Omega - \int_{\partial\Omega} \overrightarrow{t} \cdot \{\{\overrightarrow{v}^*_{node}\}[N_v]\}d\partial\Omega \\ & - \int_\Omega \{p^*_{node}\}[N_p] \cdot div\,\overrightarrow{v}\,d\Omega + \int_\Omega c\,\overrightarrow{v} \cdot \{\overrightarrow{v}^*_{node}\}[N_v]d\Omega = 0\end{aligned} \tag{2.16}$$

To eliminate the test functions of both velocity and pressure, the derivations over the $\{\overrightarrow{v}^*_{node}\}$ and $\{p^*_{node}\}$ for the Brinkman system (2.16) were calculated.

Let equation (2.16) to be the function of velocity and pressure $R(\overrightarrow{v}, p)$,

$$\begin{aligned} R(\overrightarrow{v}, p) = &\int_{\Omega} \boldsymbol{T} : \{\{\overrightarrow{v}^*_{node}\}\nabla[N_v]\}d\Omega - \int_{\partial\Omega} \overrightarrow{t} \cdot \{\{\overrightarrow{v}^*_{node}\}[N_v]\}d\partial\Omega \\ &- \int_{\Omega} \{p^*_{node}\}[N_p] \cdot div\,\overrightarrow{v}\,d\Omega + \int_{\Omega} c\overrightarrow{v} \cdot \{\{\overrightarrow{v}^*_{node}\}[N_v]\}d\Omega = 0 \end{aligned} \tag{2.17}$$

Thus the derivation of function $R(\overrightarrow{v}, p)$ (3.6) over $\{\overrightarrow{v}^*_{node}\}$ and $\{p^*_{node}\}$ are,

$$\begin{aligned} &\frac{\partial R}{\partial\{\overrightarrow{v}^*_{node}\}} = \int_{\Omega} \boldsymbol{T} : \nabla[N_v]d\Omega - \int_{\partial\Omega} \overrightarrow{t} \cdot [N_v]d\partial\Omega + \int_{\Omega} c\overrightarrow{v} \cdot [N_v]d\Omega = 0 \\ &\frac{\partial R}{\partial\{p^*_{node}\}} = -\int_{\Omega} [N_p] \cdot div\,\overrightarrow{v}\,d\Omega = 0 \end{aligned} \tag{2.18}$$

Then the solved problem for the Brinkman system is transfered to seek the root of the very matrix system:

$$\overrightarrow{r} = \begin{bmatrix} \dfrac{\partial R}{\partial\{\overrightarrow{v}^*_{node}\}} \\ \dfrac{\partial R}{\partial\{p^*_{node}\}} \end{bmatrix} = \int_{\Omega} \begin{bmatrix} \boldsymbol{T} : \nabla[N_v] + c\overrightarrow{v} \cdot [N_v] \\ -[N_p] \cdot div\,\overrightarrow{v}\,d\Omega \end{bmatrix} - \int_{\partial\Omega} \begin{bmatrix} \overrightarrow{t} \cdot [N_v] \\ 0 \end{bmatrix} = \mathbf{0} \tag{2.19}$$

To solve the numerical scheme, the Newton Raphson method was employed. It is a method for finding successively better approximations to the roots of a real-valued function. Take the formulation $\boldsymbol{F}(x_1, x_2, ..., x_i, ..., x_n) = \overrightarrow{0}$ as an example. Mark $(x_1, x_2, ..., x_i, ..., x_n)$ to be the vector $\overrightarrow{x}$. The idea of the method is as follows: one starts with an initial guess $\overrightarrow{x}^0$ which is reasonably close to the true root, then the function is approximated by its tangent line(which can be computed using the tools of calculus), and one computes the x-intercept of this tangent line(which is easily done with elementary algebra). This x-intercept will typically be a better approximation to the function's root than the original guess, and the method can be iterated [22].

It could be also explained by employing the Taylor series. For simplicity, mark each row of the formulation $\boldsymbol{F}(x_1, x_2, ..., x_i, ..., x_n) = \mathbf{0}$ to be $F_i = 0$. For all the rows of the equation,

after expanding the formulation with first degree Taylor series, the i^{th} row of the formulation could be rewritten,

$$F_i(\overrightarrow{x}^0) + (x_1^1 - x_1^0)\frac{\partial F_i}{\partial x_1}(\overrightarrow{x}^0) + ... + (x_i^1 - x_i^0)\frac{\partial F_i}{\partial x_i}(\overrightarrow{x}^0) + ... + (x_n^1 - x_n^0)\frac{\partial F_i}{\partial x_n}(\overrightarrow{x}^0) = 0 \quad (2.20)$$

where x_i^1 stands for the new value of x_i and x_i^0 is the previous value of x_i. Rearranging these formulation in matrix form,

$$\begin{bmatrix} \frac{\partial F_1}{\partial x_1} & ... & \frac{\partial F_1}{\partial x_i} & ... & \frac{\partial F_1}{\partial x_n} \\ ... & ... & ... & ... & ... \\ \frac{\partial F_i}{\partial x_1} & ... & \frac{\partial F_i}{\partial x_i} & ... & \frac{\partial F_i}{\partial x_n} \\ ... & ... & ... & ... & ... \\ \frac{\partial F_n}{\partial x_1} & ... & \frac{\partial F_n}{\partial x_i} & ... & \frac{\partial F_n}{\partial x_n} \end{bmatrix} \begin{bmatrix} x_1^1 \\ ... \\ x_i^1 \\ ... \\ x_n^1 \end{bmatrix} = \begin{bmatrix} x_1^0\frac{\partial F_1}{\partial x_1} + ... + x_i^0\frac{\partial F_1}{\partial x_i} + ... + x_n^0\frac{\partial F_1}{\partial x_n} - F_1 \\ ... \\ x_1^0\frac{\partial F_i}{\partial x_1} + ... + x_i^0\frac{\partial F_i}{\partial x_i} + ... + x_n^0\frac{\partial F_i}{\partial x_n} - F_i \\ ... \\ x_1^0\frac{\partial F_n}{\partial x_1} + ... + x_i^0\frac{\partial F_n}{\partial x_i} + ... + x_n^0\frac{\partial F_n}{\partial x_n} - F_n \end{bmatrix} \quad (2.21)$$

All the derivation and the function occurred in equation (2.21) are calculated with the initial guess $\overrightarrow{x}^0(x_1^0, ..., x_i^0, ..., x_n^0)$. And the matrix

$$\begin{bmatrix} \frac{\partial F_1}{\partial x_1} & ... & \frac{\partial F_1}{\partial x_i} & ... & \frac{\partial F_1}{\partial x_n} \\ ... & ... & ... & ... & ... \\ \frac{\partial F_i}{\partial x_1} & ... & \frac{\partial F_i}{\partial x_i} & ... & \frac{\partial F_i}{\partial x_n} \\ ... & ... & ... & ... & ... \\ \frac{\partial F_n}{\partial x_1} & ... & \frac{\partial F_n}{\partial x_i} & ... & \frac{\partial F_n}{\partial x_n} \end{bmatrix} \quad (2.22)$$

is called the Jacobean matrix $\boldsymbol{K}$.

Then the problem can be transfered to seek the root of the function $\boldsymbol{F}(\overrightarrow{x}) = \overrightarrow{0}$. By using the initial guess $\overrightarrow{x}^0$ and the given tolerance, the Newton Raphson algorithm can be described as,

while($\boldsymbol{F}(\overrightarrow{x}^i) > tolerance$)

calculate the Jacobean matrix $\boldsymbol{K}$ using equation (2.22).

update the profiles for the variables $\overrightarrow{x}^i$ using the equation (2.21).

while end;

There are a lot of ways to check the condition to end the loop, the most usual used method are by the square norm which is also used in the thesis. More accurate rules could be by the maximum value of the matrix. In this way, the algorithm could be iterated.

Starting with an initial guess $(\overrightarrow{v}^0, p^0)$, which is close to the true root. For the Brinkman system (3.7) , mark the equation of the first row of the matrix to be $\overrightarrow{r}_1$,and the equation of the second row of the matrix to be $\overrightarrow{r}_2$. Recalling that $\boldsymbol{T} = \boldsymbol{\sigma^d} - p\boldsymbol{I}$, $\boldsymbol{\sigma^d} = 2\mu\nabla^s\overrightarrow{v}$ and $\overrightarrow{v} = \{\overrightarrow{v}_{node}\}[N_v]$, $p = \{p_{node}\}[N_p]$, so

$$
\begin{aligned}
\frac{\partial \overrightarrow{r}_1}{\partial \overrightarrow{v}} &= \frac{\partial}{\partial \overrightarrow{v}}\{\int_\Omega (\boldsymbol{T} : \nabla[N_v] + c\overrightarrow{v}\cdot[N_v])d\Omega - \int_{\partial\Omega}\overrightarrow{t}\cdot[N_v]d\partial\Omega\} \\
&= \int_\Omega (\nabla[N_v]^T 2\mu\nabla[N_v] + [N_v]^T c[N_v])d\Omega \\
\frac{\partial \overrightarrow{r}_1}{\partial p} &= \frac{\partial}{\partial p}\int_\Omega \boldsymbol{T} : \nabla[N_v]d\Omega = \frac{\partial}{\partial p}\int_\Omega -p\boldsymbol{I} : \nabla[N_v]d\Omega = -\int_\Omega \nabla[N_v]^T[N_p]d\Omega \qquad (2.23) \\
\frac{\partial \overrightarrow{r}_2}{\partial \overrightarrow{v}} &= \frac{\partial}{\partial \overrightarrow{v}}(-\int_\Omega [N_p]\cdot div\overrightarrow{v}d\Omega) = -\int_\Omega \nabla[N_v]^T[N_p]d\Omega \\
\frac{\partial \overrightarrow{r}_2}{\partial p} &= \frac{\partial}{\partial p}(-\int_\Omega [N_p]\cdot div\overrightarrow{v}d\Omega) = 0
\end{aligned}
$$

Take equation (2.21), and let $\boldsymbol{F}$ to be $\overrightarrow{r}$ and n to 2, it could be rewritten as,

$$
\begin{bmatrix} \frac{\partial \overrightarrow{r}_1}{\partial \overrightarrow{v}} & \frac{\partial \overrightarrow{r}_1}{\partial p} \\ \frac{\partial \overrightarrow{r}_2}{\partial \overrightarrow{v}} & \frac{\partial \overrightarrow{r}_2}{\partial p} \end{bmatrix} \begin{bmatrix} \overrightarrow{v} \\ p \end{bmatrix} = \begin{bmatrix} \overrightarrow{v}^0\frac{\partial \overrightarrow{r}_1}{\partial \overrightarrow{v}} + p^0\frac{\partial \overrightarrow{r}_1}{\partial p} - \overrightarrow{r}_1 \\ \overrightarrow{v}^0\frac{\partial \overrightarrow{r}_2}{\partial \overrightarrow{v}} + p^0\frac{\partial \overrightarrow{r}_2}{\partial p} - \overrightarrow{r}_2 \end{bmatrix} \qquad (2.24)
$$

Therefore the Jacobean matrix for the Brinkman system is obtained as,

$$
\boldsymbol{K} = \int_\Omega \begin{bmatrix} \nabla[N_v]^T 2\mu\nabla[N_v] + [N_v]^T c[N_v] & -\nabla[N_v]^T[N_p] \\ -[N_p]^T\nabla[N_v] & 0 \end{bmatrix} \qquad (2.25)
$$

Up to now, the Newton Raphson iteration algorithm has been illustrated for the Brinkman system. It can be solved by using the numerical scheme (2.15), the Newton Raphson iteration scheme (2.24) and the Jacobean matrix (2.25).

2.4 Stability and Interpolation

The problem of stability in FE methods in fluid mechanics was early analyzed by Ladyzhenskaya, Babouska and Brezzi, who gave their names to the so-called Ladyzhenskaya, Babouska and Brezzi (LBB) stability condition. Their work focuses on the Stokes equations and they demonstrated the need, in fluid mechanics FE methods, for using different basis functions for the velocity and pressure. This was equivalent to staggering the grid in space, as was done for the FD methods. Furthermore, not any combination of basis functions satisfies the LBB condition. Arnold and Fortin emphasized that one simple way to stabilize equal-order schemes is to add the so-called bubble function, and that this method does not lead necessarily to an additional cost, thanks to static condensation techniques (some easy manual Gaussian elimination before solving numerically the matrix problem). But, since, according to Pierre, these methods are equivalent to adding a penalty term in the fluid equations, they may be over-dissipative in the context of unsteady flows and the more general Navier-Stokes equations [14].

Starting from the definition of the $L^2(\Omega)$ space and the Sobolev space $H^1(\Omega)$. $L^2(\Omega)$ space is defined as,

$$L^2(\Omega; R) = \{h = h(\overrightarrow{x}) : \int_\Omega |h(\overrightarrow{x})|^2 d\Omega < \infty\} \tag{2.26}$$

where $\overrightarrow{x}$ represents the space. And the Sobolev space $H^1(\Omega)$ is defined as,

$$H^1(\Omega) = \{v \in L^2 : \nabla v \in L^2\} \tag{2.27}$$

And $H_0^1(\Omega)$ is the standard notation for the Sobolev space of vector-valued functions that are square integrable, with square integrable first derivatives, and with zero trace on $\partial\Omega$, while the space $L_0^2(\Omega)$ is defined as,

$$L_0^2(\Omega) = \{q \in L^2(\Omega) : \int_\Omega q d\Omega = 0\} \tag{2.28}$$

The norm in $L^2(\Omega)$ space is defined as $\| u \|_{L^2} = (\int_\Omega |u|^2 d\Omega)^{\frac{1}{2}}$, while the norm in Hilbert space is defined as $\| u \|_{H^1} = (u,u)_{H^1}^{\frac{1}{2}} = (\int_\Omega |u|^2 d\Omega + \int_\Omega \nabla u \cdot \nabla u d\Omega)^{\frac{1}{2}}$. With the mixed finite element method used above, take two triangulations $\{\Gamma_{h_p}\}$ and $\{\Gamma_{h_{\overrightarrow{v}}}\}$ of Ω for example, the continuous piecewise finite element: $P_k - P_{k'}$ element for $(\overrightarrow{v}_h, p_h)$ should be,

$$\begin{aligned} X_{h_v} &= \{\overrightarrow{v} \in (C^0(\Omega))^d : \forall K \in \Gamma_{h_{\overrightarrow{v}}}, \overrightarrow{v} \in (P_k)^d\} \\ M_{h_p} &= \{q \in C^0(\Omega) : \forall K \in \Gamma_{h_p}, q \in P_k^{'}, \int_\Omega q = 0\} \end{aligned} \tag{2.29}$$

Thus the problem for the steady Brinkman system without external force now is transfered to be:

Find $\overrightarrow{v}_h \in X_{h_v}$ and $p_h \in M_{h_p}$

$$\begin{cases} \forall \overrightarrow{v} \in X_{h_v}, & a_{h_v}(\overrightarrow{v}_h, \overrightarrow{v}) + b_{h_v}(\overrightarrow{v}, p_h) = 0, \\ \forall q_h \in M_{h_p}, & b_{h_v}(\overrightarrow{v}_h, q_h) = 0 \end{cases} \tag{2.30}$$

where

$$\begin{cases} a_{h_v}(\overrightarrow{v}_h, \overrightarrow{v}) = \sum\limits_{K \in \Gamma_{h_v}} \int_K \nabla \overrightarrow{v} \cdot \nabla \overrightarrow{v}_h d\Omega + \sum\limits_{K \in \Gamma_{h_v}} \int_K c \overrightarrow{v} \cdot \overrightarrow{v}_h d\Omega \\ b_{h_v}(\overrightarrow{v}_h, q_h) = -\sum\limits_{K \in \Gamma_{h_v}} \int_K q_h div(v) d\Omega \end{cases} \tag{2.31}$$

The second term for a_{h_v} is for the Brinkman system. It has been proved that the both the Stokes system and Brinkman system satisfy the inf-sup condition [15],

$$0 < \beta_{h_v,h_p} = \inf_{q_h \in M_{h_p}} \sup_{\overrightarrow{v} \in X_{h_v}} \frac{b_{h_v}(\overrightarrow{v}, q_h)}{\| \overrightarrow{v} \|_{X_{h_v}} \| q_h \|_{M_{h_p}}} = \inf_{q_h \in M_{h_p}} \sup_{\overrightarrow{v} \in X_{h_v}} \frac{(div \overrightarrow{v}, q_h)}{\| \overrightarrow{v} \|_{X_{h_v}} \| q_h \|_{M_{h_p}}} \tag{2.32}$$

Which means the systems could be stable.

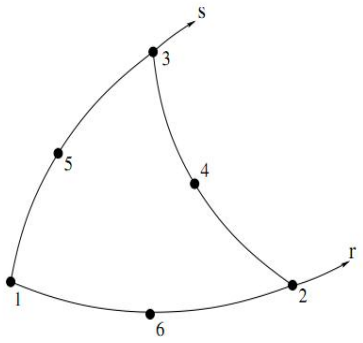

Figure 2.2 The node placement and numbering in the P2 element

The shape function used to discretize the weak formulation of the system is also called interpolation function.The finite element interpolation is such that both of the variables are treated as nodal variables so that the continuity conditions can be used during the assembly elements. Thus an element with two nodes (which is the minimum) will have unknowns (u and du/dx at each of the two nodes of the element), requiring a four-term polynomial. The mesh used in the code is the P2-P1 triangular elements which is shown in figure 2.2. The velocity are represented by the values at the six nodes per element. The pressure is represented by the three corner nodal values. It has been proved that the inf-sup condition can not be verified if the velocity and the pressure are imposed the same order of shape functions. That means the interpolation of the velocity should at least one degree higher than that of the pressure. And there is another kind of element called isoparametric element that is not only the velocity and the pressure but also the coordinates value at the node is also interpolated by the interpolation functions [16].The advantages of isoparametric elements include the ability to map more complex shapes and have compatible geometries. In addition, there is no need to distinguish between straight and curved boundaries of isoparametric elements. The disadvantages of isoparametric elements are the possibility of poor (overstiff) performance of low order isoparametric elements and

the limited use of isoparametric elements for solving plate bending and shell problems. The completeness condition for plate bending and shell problems (which have a higher variational index, greater than 1) is not satisfied using isoparametric formulation [17].

2.5 The Level Set method

During the work, the level set method was used to distinguish the layers of the material and also to research the propagation of the flow front. The basic idea is as following, the flow front was prescribed to be the iso-zero of a level set field $\phi(\overrightarrow{x}(t), t)$. Usually, ϕ represents the signed distance to this flow front and it is defined as:

$$\phi(\overrightarrow{x}) = \min|\overrightarrow{x} - \overrightarrow{x_I}| \qquad \forall \overrightarrow{x_I} \in \partial\Omega \tag{2.33}$$

This level set function ϕ depends on both space $\overrightarrow{x}(t)$ and time t while the space $\overrightarrow{x}(t)$ also depends on time t. Firstly, as it depends on the space $\overrightarrow{x}(t)$, by evaluating the sign of $\phi(\overrightarrow{x}_{given}, t_{given})$ from a given point $\overrightarrow{x}_{given}$ at a given time t_{given}, it could be known which side is the point at the level set. Take an easy case, if the level set is a circle, so simply, it could be known if the given point is inside or outside the circle or level set.

Secondly because the level set function also depends on the time, thus to investigate the propagation of the flow front with the time t, the derivation of the flow front over time was calculated as equation (2.34)

$$\frac{d}{dt}\phi(\overrightarrow{x}(t), t) = 0 = \frac{\partial\phi}{\partial t} + \frac{\partial\phi}{\partial\overrightarrow{x}}\frac{\partial\overrightarrow{x}}{\partial t} = \frac{\partial\phi}{\partial t} + \overrightarrow{\nabla}\phi \cdot \overrightarrow{v} \tag{2.34}$$

Initially, the position of the flow front was prescribed as $\phi(\overrightarrow{x}, 0)$, and the initial condition also provide a initial velocity field $\overrightarrow{v}^0$. The normal of the curve is prescribed as,

$$\overrightarrow{n} = \frac{\overrightarrow{\nabla}\phi}{|\overrightarrow{\nabla}\phi|} \tag{2.35}$$

After imposing the normal vector to the equation (2.34), it could be obtained,

$$\overrightarrow{\nabla}\phi \cdot \overrightarrow{v} = |\overrightarrow{\nabla}\phi| \frac{\overrightarrow{\nabla}\phi}{|\overrightarrow{\nabla}\phi|} \cdot \overrightarrow{v} = |\overrightarrow{\nabla}\phi| \overrightarrow{n} \cdot \overrightarrow{v} = |\overrightarrow{\nabla}\phi| v_n \tag{2.36}$$

Thus,

$$\frac{d}{dt}\phi(\overrightarrow{x}(t), t) = 0 = \frac{\partial \phi}{\partial t} + \overrightarrow{\nabla}\phi \cdot \overrightarrow{v} = \frac{\partial \phi}{\partial t} + |\overrightarrow{\nabla}\phi| v_n \tag{2.37}$$

Equation (2.37) shows the importance of the normal velocity v_n in the propagation of the flow front. As shown in figure 2.3, without normal velocity of the level set, the level set would not be able to propagate.

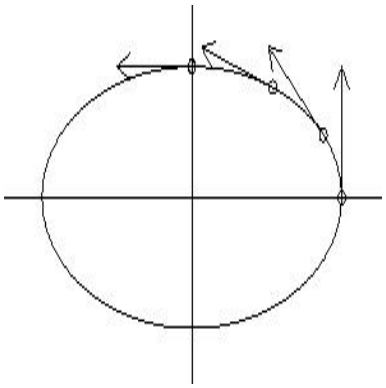

Figure 2.3 The level set without the normal velocity

To compute the propagation of the flow front, the Hamilton-Jacobean method [20] was employed.The HamiltonJacobean equation is a first-order, non-linear partial differential equation for a function called Hamilton's principal function

$$H(q_1, ..., q_N; \frac{\partial S}{\partial q_1}, ..., \frac{\partial S}{\partial q_N}) + \frac{\partial S}{\partial t} = 0 \tag{2.38}$$

Thus the equation 2.28 and the derived equation 2.30 are the typical Hamilton-Jacobean equation, they could be rewritten as,

$$\frac{\partial \phi}{\partial t} + H(\nabla \phi) = 0 \tag{2.39}$$

where ϕ is the contour of the level set. Actually by integrating the conservation law in space, the Hamilton-Jacobean equation could be obtained.

To solve the numerical scheme of (2.39), the CFL condition is imposed to calculate the time step during the propagation [21]. It is a condition to set the maximum time step. A condition number called CFL was imposed to be less than 0.5,

$$\begin{aligned} CFL &= \frac{\parallel v \parallel \Delta t}{h_e} < 0.5 \\ \Rightarrow \Delta t &= \frac{1}{2}\frac{h_e}{\parallel v \parallel} \end{aligned} \tag{2.40}$$

where h_e is the element size, $\parallel v \parallel$ is the normal velocity of the flow front. As with this time step, the interface can not move forward a complete element, it ensures the stability of the solution. After the propagation of the level set, the property $\parallel \phi \parallel = 1$ is no longer ensured, which leads the level set not able to represent the distance anymore. Although the iso-zero values of the level set still describes the interface, the $\parallel \phi \parallel = 1$ is still needed to be ensured. Because it is useful to avoid the numerical divergence. For this reason, the reinitialization of the level set is done after the propagation of the level set.

By calculating the gradient, the equation (2.34) could be rewritten as,

$$\frac{\partial \phi}{\partial t} + v_x \frac{\partial \phi}{\partial x} + v_y \frac{\partial \phi}{\partial y} = 0 \tag{2.41}$$

The problem has to be solved numerically which means the problem has to be discretized firstly. The numerical scheme used for the equation (2.41) depends on the sign of the velocity. For the first order and an explicit upwind scheme of 2 dimensional case, the derivation over time could be discretized as,

$$\frac{\partial \phi}{\partial t} = \frac{\phi_{ij}^{n+1} - \phi_{ij}^{n}}{\Delta t} \tag{2.42}$$

where the lower index i and j indicate the point in the domain and the upper index indicate the the current iteration step, Δt is the time step. While for the derivation of ϕ over space, it depends on the sign of the velocity, at point i, j,

if $v_{x,ij} > 0$, then the first order upwind approximation of $v_x \dfrac{\partial \phi}{\partial x}$

$$\frac{\partial \phi_{i,j}^n}{\partial x} = \frac{\phi_{i,j}^n - \phi_{i-1,j}^n}{\Delta x}$$

else

$$\frac{\partial \phi_{i,j}^n}{\partial x} = \frac{\phi_{i,j}^n - \phi_{i-1,j}^n}{\Delta x}$$

The same for the approximation of $v_y \dfrac{\partial \phi}{\partial y}$

if $v_{y,ij} > 0$

$$\frac{\partial \phi_{i,j}^n}{\partial x} = \frac{\phi_{i,j}^n - \phi_{i-1,j}^n}{\Delta x}$$

else

$$\frac{\partial \phi_{i,j}^n}{\partial x} = \frac{\phi_{i,j}^n - \phi_{i-1,j}^n}{\Delta x}$$

The scheme presented above is just an very simple example of the discretization of the level set propagation equation. There are a lot of more accurate schemes like Essentially non-oscillatory scheme (ENO) scheme and Weighted ENO (WFNO) scheme. The first ENO scheme is constructed by Harten et. al. in 1987. The first WENO scheme is constructed in 1994 by Liu,Osher and Chan for a third order finite volume version. In 1996, third and fifth order finite difference WENO schemes in multi space dimensions are constructed by Jiang and Shu, with a general framework for the design of smoothness indicators and nonlinear weights [18]. By using these kinds of theories, the propagation of the flow front could be studied.

Chapter 3

Results and Discussion

3.1 Single Domain test

3.1.1 Verify with Stokes system

Several tests were made for both cases, and the results were also compared with that of the commercial software COMSOL.The first tested mesh is a 2D square homogenized mesh shown as in figure 3.1.

The domain is a simple square with a rather coarse homogeneous mesh. The length of the square is 1 meter, and the origination is at the center of the square. The coarse homogeneous mesh is used here because the domain is simple and the solution is expected to be not mesh sensitive. The first test was made to compare the results between the Brinkman system and the Stokes system. In this case, the resin enter the cavity from the top of the domain and gets out of the cavity from the right side. To do that, the left side and the bottom of the domain is closed and bounded while the right side of the domain is totally free. At the top of the square, the velocity of $(0, -1, 0)$ was imposed with the unit of m/s. That means the

resin enter the cavity vertically. Thus the boundary conditions are:

- $\overrightarrow{v} \cdot \overrightarrow{e}_y = 0$ at the bottom;
- $\overrightarrow{v} \cdot \overrightarrow{e}_x = 0$ at the left side;
- $\overrightarrow{v}(y) = -1$ at the top

For the Stokes system, the profiles of velocity, pressure and the divergence of velocity is shown in figure 3.2. As it can be seen from figure 3.2(a), the norm of the velocity is zero at the left bottom corner while it get the maximum value of 1.41 at the right top corner. The incompressibility condition is satisfied perfectly which could be proved by the magnitude of the $div\,\overrightarrow{v}$ to be 10^{-13} from figure 3.2(c). The pressure is homogeneous which means the gradient of the pressure should be zero.

Then the test is performed with the Brinkman formulation. Comparing the equation (2.4) and (2.6), setting the drag coefficient $c = \dfrac{\mu_e}{k}$ to be zero which means the μ_e is set to be zero will make the two equations are exactly the same. Results were then checked to be exactly the same as for the Stokes system. Figure 3.3 presents the same results as for the Stokes case but including now a drag coefficient c based on a given permeability k.

To test the influence of the permeability, the dynamic viscous μ_e was kept $1Pa \cdot s$ for all of the next tests, while the value of the permeability changes from $0.00001m^2$ to $1m^2$ with the change rate of 10. After moving through the whole domain, the velocity of the resin at the bottom is sufficient influenced by the permeability of the resin. As the y velocity of the resin was prescribed to be zero. The profile of the x velocity at the bottom of the domain was obtained for different permeabilities. They are shown in figure 3.4.

Recalling the physical meaning of the permeability, it is the ratio of the space inside the domain to the solid part. Thus, it could be predicted that the bigger the permeability, the easier the flow could move through the domain. That is the relation between the velocity and the permeability is proportional. Figure 3.4 shows that generally the velocity increases when the permeability increases, but when the magnitude of the permeability is smaller than 10^{-4}, the velocity after point $(0.25, -0.5)$ will decrease. This is because of the influence of the Brinkman term increases to be more than the summation of the influence of all other three terms. Figure 3.5 shows the results of the $div\,\overrightarrow{v}$ for different permeabilities. Similarly as the Stokes test, because the system for the porous medium is a mixed formulation of Brinkman equation and the mass conservation, the incompressibility condition should be satisfied. From the comparison of the graphs in figure 3.5, the incompressibility condition is almost satisfied, while it is getting worse with the increase of the permeability which increases the influence of the Brinkman term. Therefore, it can be concluded that the incompressibility condition will never be exactly satisfied in practice at the local(elements) scale but only at the macroscopic(part) scale.

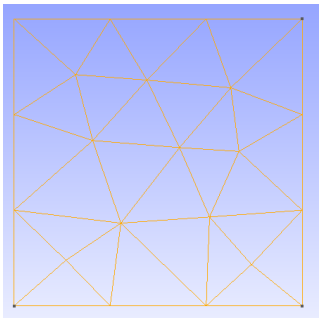

Figure 3.1 The homogeneous mesh

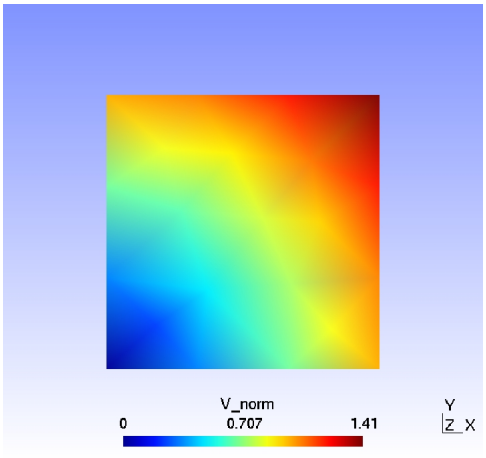

(a) norm velocity

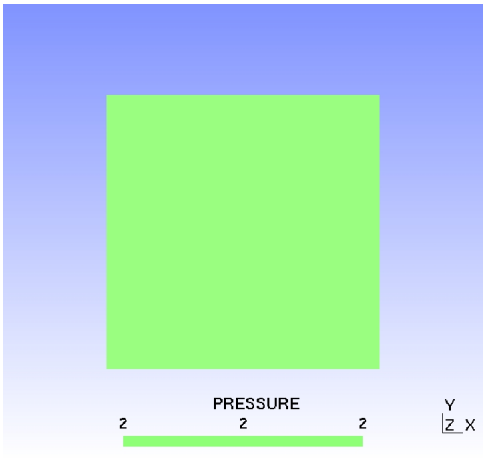

(b) pressure

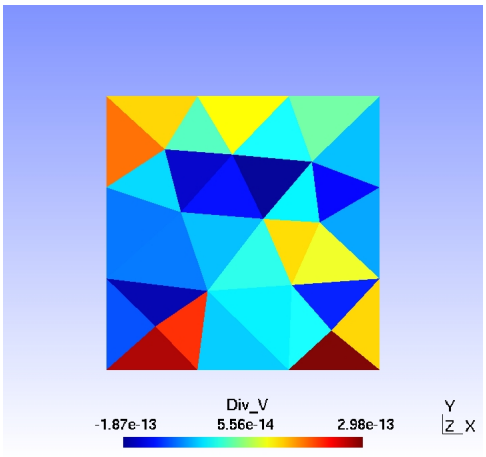

(c) velocity divergence

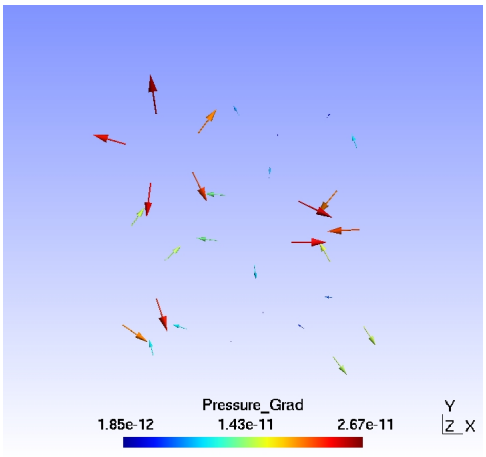

(d) pressure gradient

Figure 3.2 results of the Stokes system

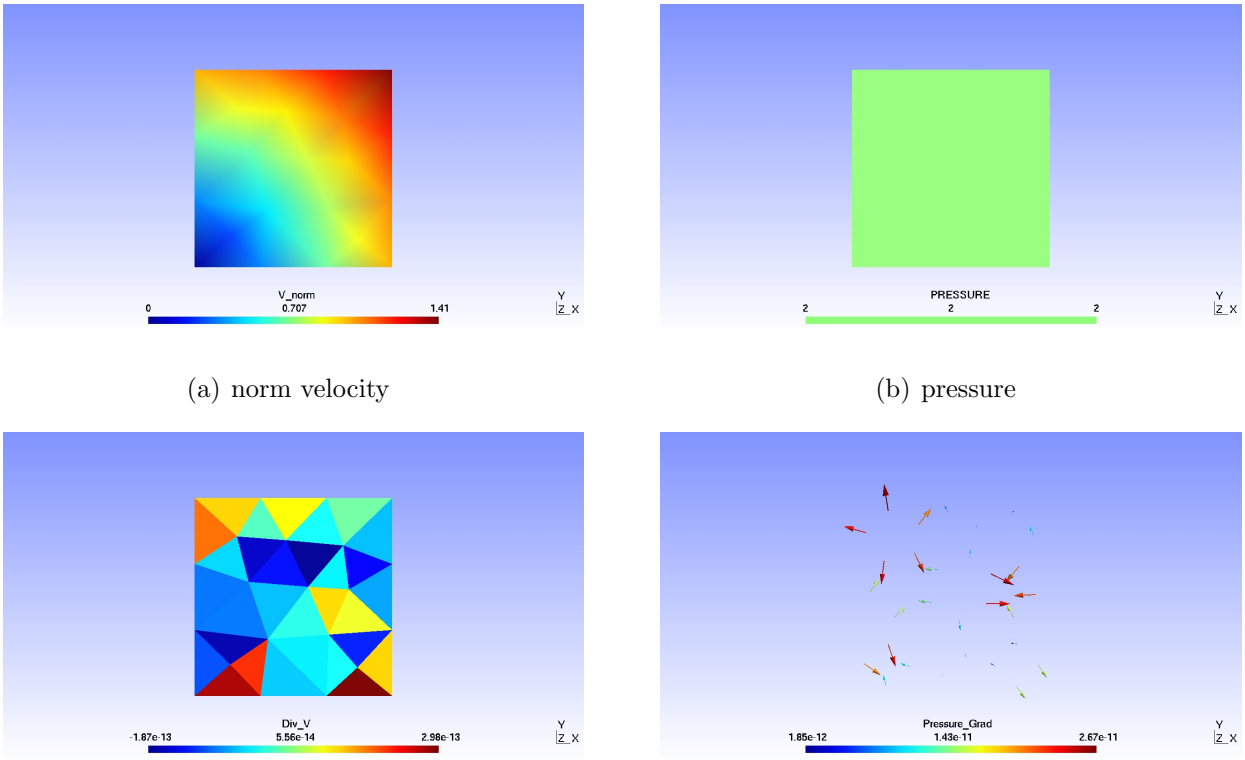

(a) norm velocity

(b) pressure

(c) velocity divergence

(d) pressure gradient

Figure 3.3 results of the Brinkman formulation

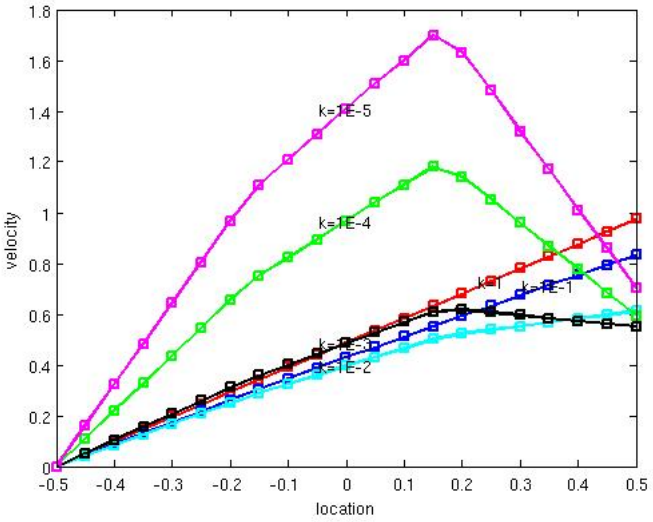

Figure 3.4 The velocity profiles at the bottom for different permeabilities

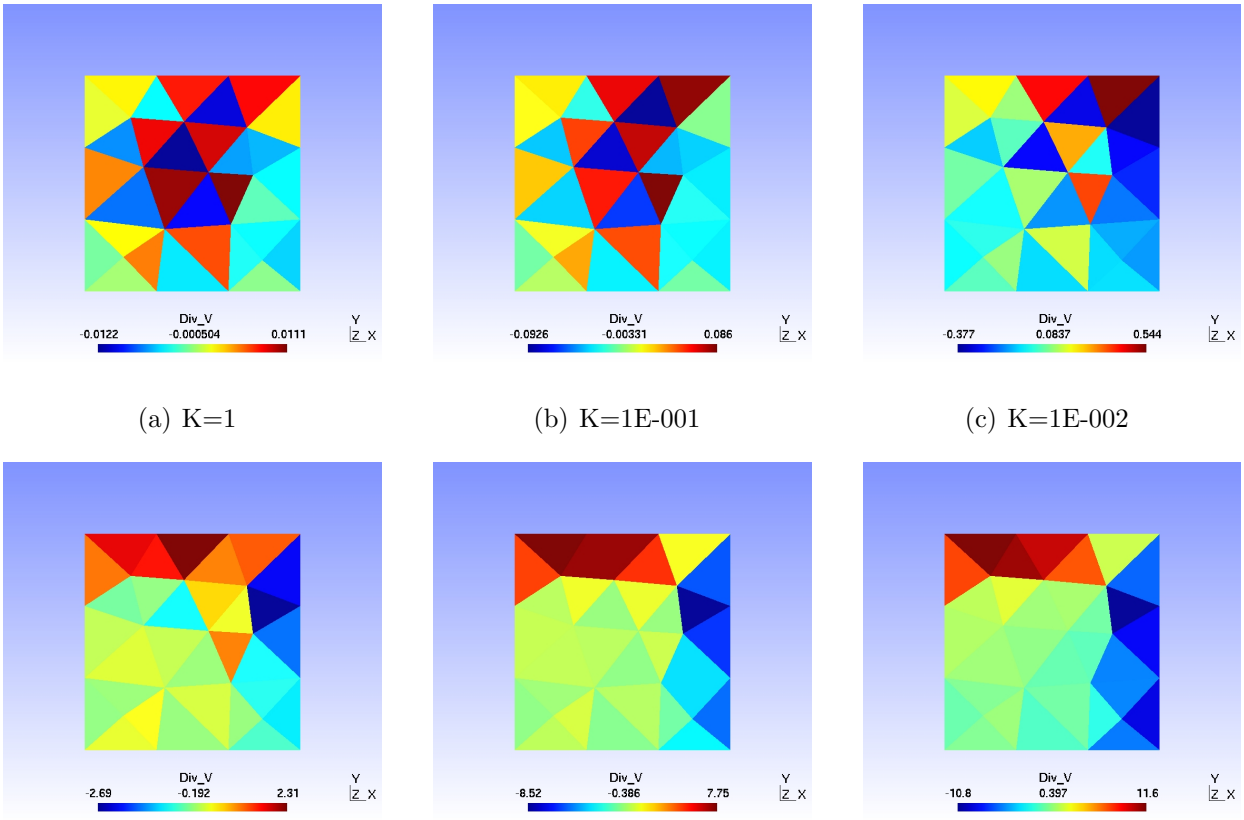

(a) K=1 (b) K=1E-001 (c) K=1E-002

(d) K=1E-003 (e) K=1E-004 (f) K=1E-005

Figure 3.5 divergence of the velocity field for different permeabilities

3.1.2 Filtration test

We now aim to simulate a standard filtration test in order to analytically check the Brinkman formulation. In this case, the resin is assumed to enter the cavity from the left side with the velocity only along x direction. Therefore, a slim mold with a length of $3m$ and the width of $1m$ was built. It is shown in figure 3.6. This slim body could increase the time of the flow to stay inside the mold. That will enhance the effects of the capillary pressure.

The resin passes from the left to the right of the domain. Instead of imposing velocity simply as the previous test, the pressure difference between the the left and the right side was imposed to provide the driven force for the flow. However, as the body is slim along x direction, it is better to enable the flow get a rather bigger velocity along x direction than the y direction. To do that, the y component of the velocity was prescribed to be zero at the both sides. The top and the bottom was bounded. Thus the boundary conditions were prescribed as:

- $\overrightarrow{v} \cdot \overrightarrow{e}_y = 0$ at the bottom;
- $\overrightarrow{v} \cdot \overrightarrow{e}_y = 0$ at the top;
- $\overrightarrow{v} \cdot \overrightarrow{e}_y = 0$ and $\boldsymbol{\sigma} \cdot \overrightarrow{n} = \overrightarrow{t} = 0Pa$ at the right side ;
- $\overrightarrow{v} \cdot \overrightarrow{e}_y = 0$ and $\boldsymbol{\sigma} \cdot \overrightarrow{n} = \overrightarrow{t} = 10000Pa$ at the left side ;

The slip condition here should be taken into account. The reason would be figured out later. For this reason, the whole tests were divided into two parts: the slip case and the no slip case at the top and the bottom. For both tests, the constants are prescribed as table 3.1.

The first part of the test is for the 1D filtration mold for which the slip condition was imposed at the top and bottom of the domain. That is

Table 3.1 Constants for the filtration test

viscosity	intrinsic viscosity	permeability
0.1	0.1	1.0E-3

- $\overrightarrow{v}(x)$ is free at the bottom and the top

Together with the boundary condition described above, the problem was solved with results shown in figure 3.7.

This result is perfect. The x component of the velocity and the gradient of the pressure are homogeneous while the y component for both are zero. And the magnitude of the divergence of the velocity is 10^{-10}. That means the incompressibility condition is satisfied very well.

The second part is with the no slip condition imposed at both the top and the bottom of the domain. That is:

- $\overrightarrow{v} \cdot \overrightarrow{e}_x = 0$ at both the bottom and the top

Together with the boundary condition described above, the results are given figure 3.8. Comparing this with the results of the 1D filtration case, the results are almost the same with the difference occurred at the bottom and the top boundary of the domain. For the velocity and the gradient of the pressure, they are homogeneous all over the domain except at the boundary. It could be noticed with Gmsh that the magnitude of the divergence of the velocity field is -10 in the middle part but reached -1 at the boundary. The incompressibility condition was not guaranteed at the both boundaries. These could be all explained by the imposed zero velocity at the both boundaries. There are some discontinuous or sharp change, if preferred, perpendicular to the both boundaries. Thus the middle part is almost the same as before while the problem for this case mainly focus on the both boundaries.

Similarly, as to check the influence of the Darcy term or the influence of the permeability, a group of tests were performed with the permeabilities varied from $0.0001m^2$ to $1m^2$. The results are shown in figure 3.9.

In the four graphs, the magnitude of the divergence of the velocity are all almost 1 which impresses the incompressibility condition were not satisfied at all. However, it can be observed that the magnitude of the $div\overrightarrow{v}$ in the middle part of the domain could be 10^{-10} which is close to that of the 1D filtration test. The big magnitude mainly occurs along the boundary. On the other hand, when the permeability decreases from 1 to 0.001, the value of $div\overrightarrow{v}$ increases. This is because the drag coefficient c increases when the permeability k decreases. Thus the influence of the Darcy term increases which make the incompressibility condition more difficult to be satisfied.

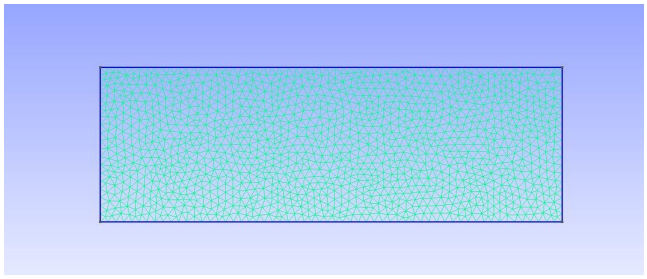

Figure 3.6 the mesh of the filtration test

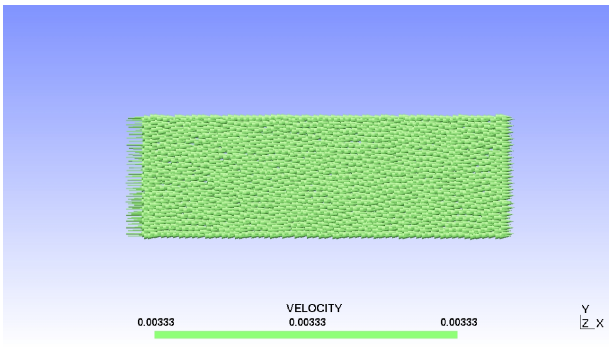

(a) velocity

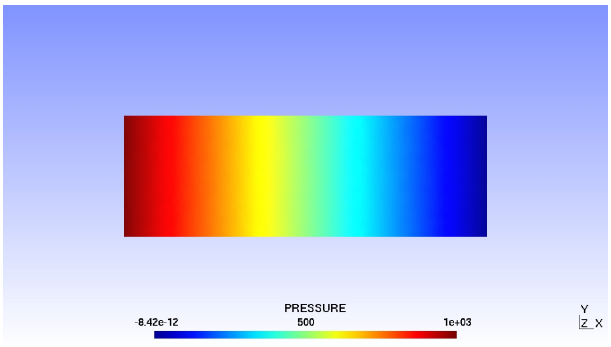

(b) pressure

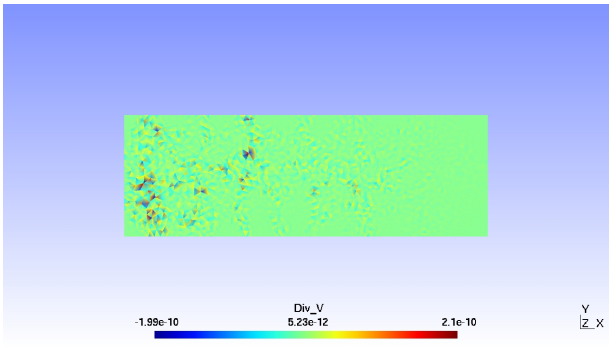

(c) velocity divergence

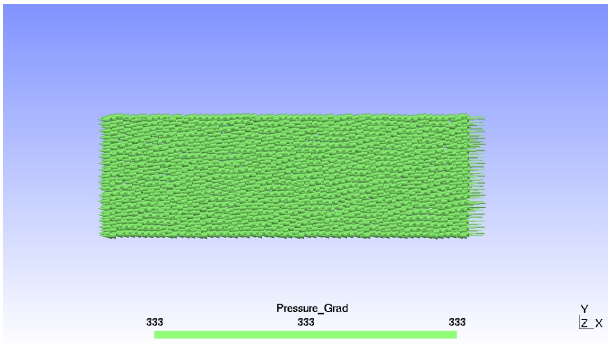

(d) pressure gradient

Figure 3.7 results of the 1D filtration test with slip condition on the upper and lower boundaries

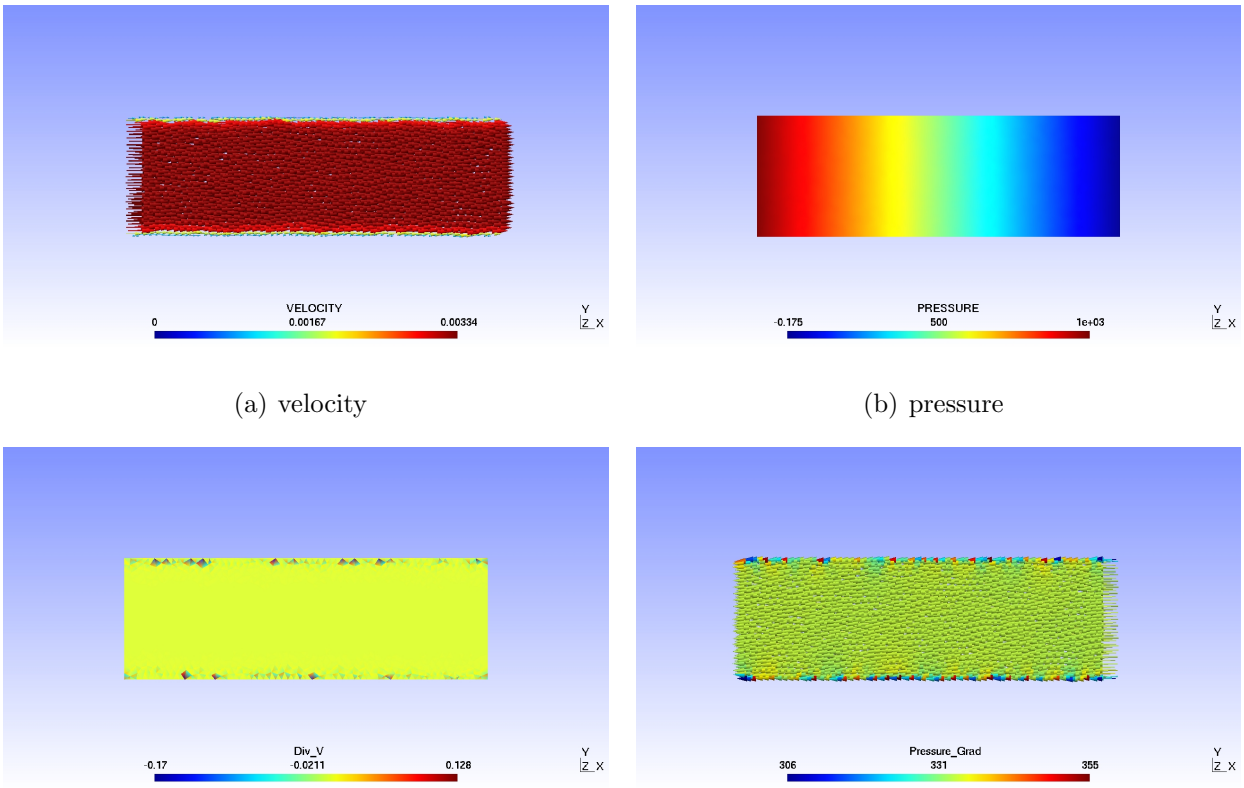

(a) velocity

(b) pressure

(c) velocity divergence

(d) pressure gradient

Figure 3.8 results of the filtration test with no slip condition on the upper and lower boundaries

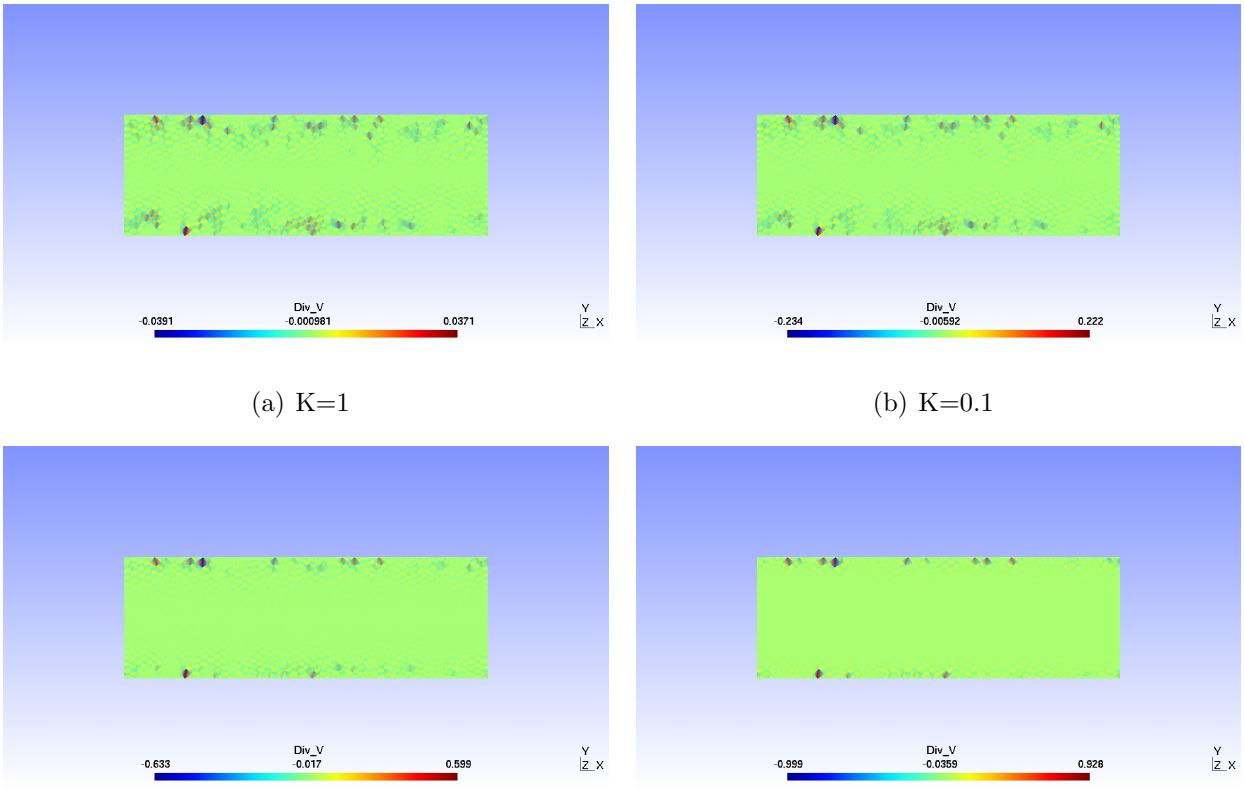

(a) K=1

(b) K=0.1

(c) K=0.01

(d) K=0.001

Figure 3.9 divergence of the velocity field for different permeability

3.1.3 3D test

Practically, there is no 2D model in the real world while some cases could be simply modeled as 2D models based on some theories. Thus it is interesting to test a simple 3D case based on the tests before. To do that, a simple 3D model was imposed with the dimension of 6 meters, 2 meters and 2 meters. Considering the computation power of the pc in the university, a rather coarse mesh was constructed with the length of the element of $0.25m$. The imposed mesh is shown in figure 3.10.

All the basic things are the same as the filtration test. In the same way as before, the model was also imposed mush longer in one dimension than the other two. Here is 3 times. The boundary condition is also the same as the 2D capillary test. The difference is the stress and the spressure are now imposed on the surface instead of imposed on the line. To focus the test on one dimension, here x direction, the velocity along other two dimensions were prescribed to be zero. According to the figure 3.10, the boundary condition could be described as:

- $\overrightarrow{v} \cdot \overrightarrow{e}_y = 0$ at the front and back surface;
- $\overrightarrow{v} \cdot \overrightarrow{e}_z = 0$ at the bottom and top surface;
- $\overrightarrow{v} \cdot \overrightarrow{e}_y = 0$, $\overrightarrow{v} \cdot \overrightarrow{e}_z = 0$ and $\boldsymbol{\sigma} \cdot \overrightarrow{n} = \overrightarrow{t} = 0Pa$ at the right side ;
- $\overrightarrow{v} \cdot \overrightarrow{e}_y = 0$, $\overrightarrow{v} \cdot \overrightarrow{e}_z = 0$ and $\boldsymbol{\sigma} \cdot \overrightarrow{n} = \overrightarrow{t} = 10000Pa$ at the left side ;

Similarly, two parts of simulation were carried out here according to the presence of no slip condition. During the first test, the no slip condition was imposed for the top, bottom front and back surfaces.

- $\overrightarrow{v} \cdot \overrightarrow{e}_z = 0$ at the front and back surface;
- $\overrightarrow{v} \cdot \overrightarrow{e}_y = 0$ at the bottom and top surface;

The results are obtained in figure 3.12.

Then the slip condition case was also carried out with the rest boundary condition as,

- $\overrightarrow{v}(z)$ is free at the front and back surface;
- $\overrightarrow{v}(y)$ is free at the bottom and top surface;

The results are plotted in figure 3.11.

For the filtration case, the velocity and the pressure gradient are both homogeneous with the pressure only changes along the x direction. The divergence of the velocity is about 10^{-10} which is really good. As illustrated earlier in this section, the mesh here is actually rather coarse, thus up to now it could be concluded that the filtration test is not mesh sensitive and the result for this case is perfectly consistent with the theoretical part.

In figure 3.12, the result of the no slip condition case, as to observe the dispersion of the profile more clear, the view of the velocity profile was adjusted to be along x direction. It is so distinct of the two cycles of blue lines around the velocity profile. And it also could be seen from the divergence profile, almost the whole domain is homogeneous while huge sharp changes occurred close to the boundary.

The same phenomenon as in 2D simulation are obtained here, magnified divergence to a rather coarse mesh, but 3D simulations seem to work perfectly.

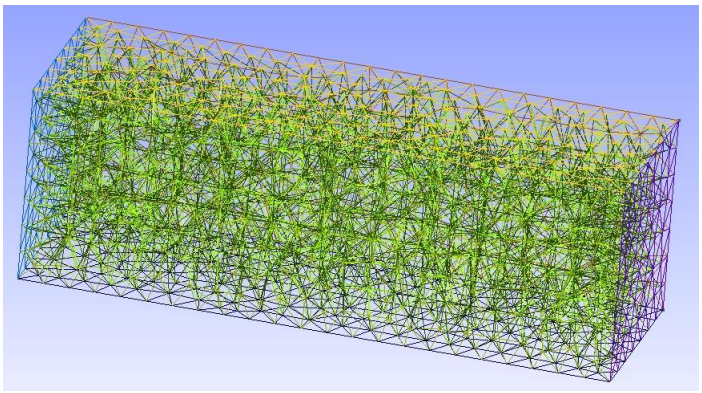

Figure 3.10 The 3D mesh

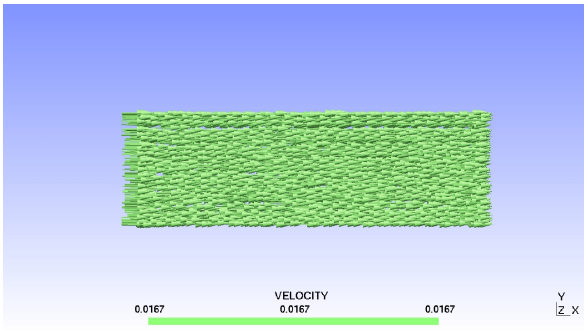

(a) velocity

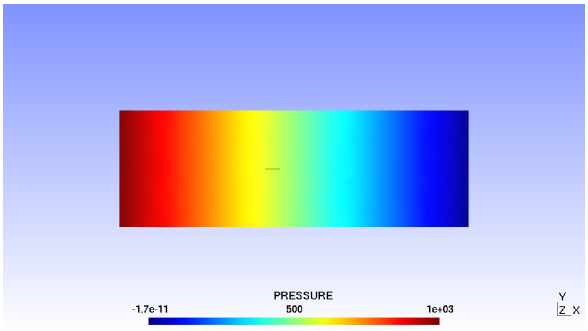

(b) pressure

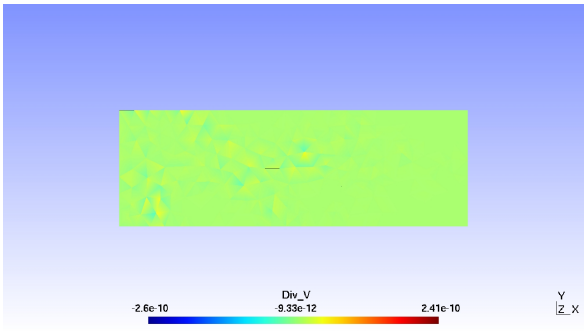

(c) velocity divergence

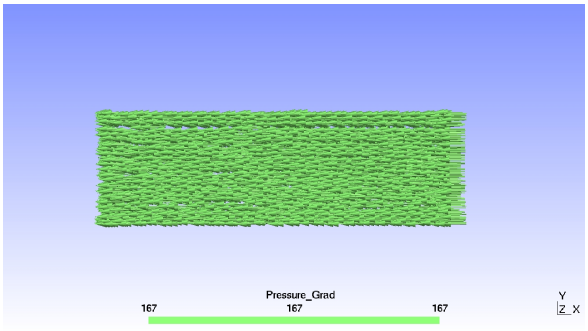

(d) pressure gradient

Figure 3.11 Results of slip condition case for 3D mesh

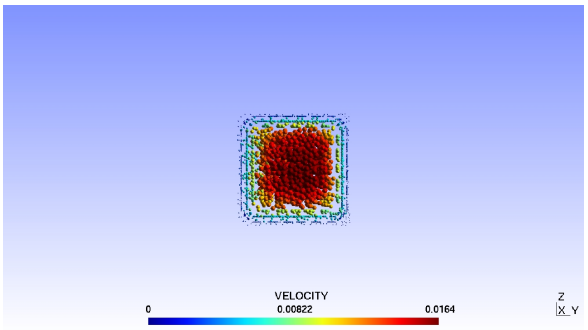

(a) velocity

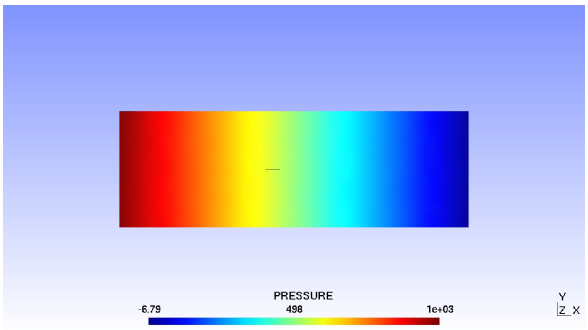

(b) pressure

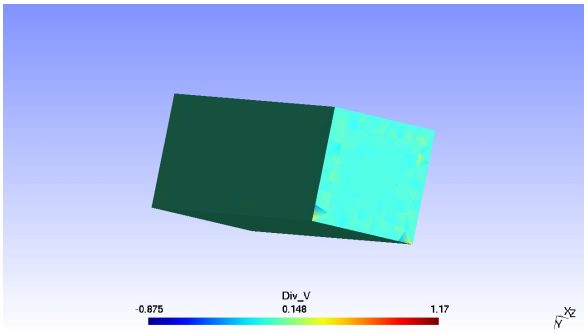

(c) velocity divergence

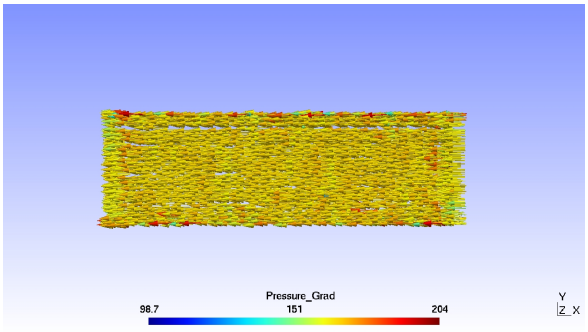

(d) pressure gradient

Figure 3.12 Results of no slip condition case for 3D mesh

3.1.4 Finer mesh test

Up to now, for the investigation of the capillary pressure, two cases were carried out: slip condition and no slip condition with both 2D and 3D mehs. The solution works perfectly for the slip condition case while there are problems at the boundary of the domain for the no slip condition case. Thus it is interesting to make a simulation with a non-homogeneous mesh with finer element at the boundary but coarse in the middle part. The dimension of the domain are $9m \times 1m$. The element size was linearly interpolated along y direction with $0.01m$ at the top and the bottom but $0.1m$ in the middle part of the domain. The mesh is shown in figure 3.13.

The no slip condition was imposed for the finer mesh simulation with exactly the same boundary condition imposed before for the capillary pressure test. The result is shown in figure 3.14.

By using Gmsh, the profiles of the velocity, the $div\,\overrightarrow{v}$ and the gradient of pressure were handled a little bit. Comparing figure 3.14 with 3.9, the velocity for the whole domain varies from 0.011 to 0.01111 which is almost homogeneous, and main problem is still at the boundary but it is much smaller than that of 3.9. The magnitude of the divergence of the velocity field is 10^{-7} even still with the problem at the boundary. This is also much smaller than that of before. The figure 3.14(d), the pressure gradient, was gotten by Gmsh with the value scale from 111.1099 to 111.12.

The result is obvious much better than that of before. That means the solution is mesh sensitive. It could be expected that the finer the mesh, the better will be the result. With powerful computer, the solution could get excellent result.

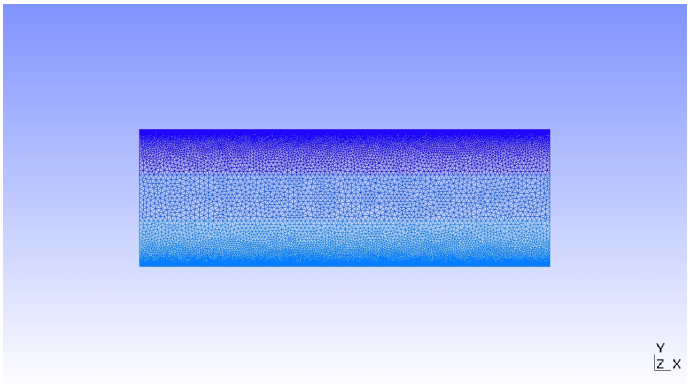

Figure 3.13 The finer mesh

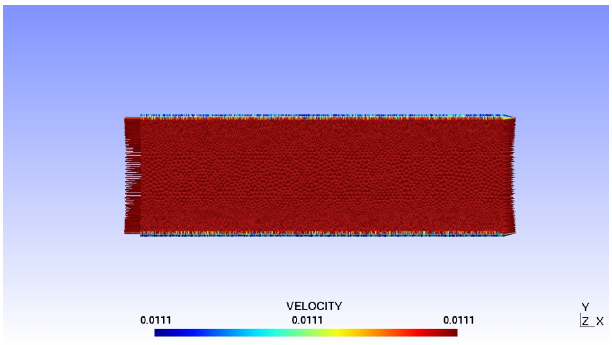

(a) velocity

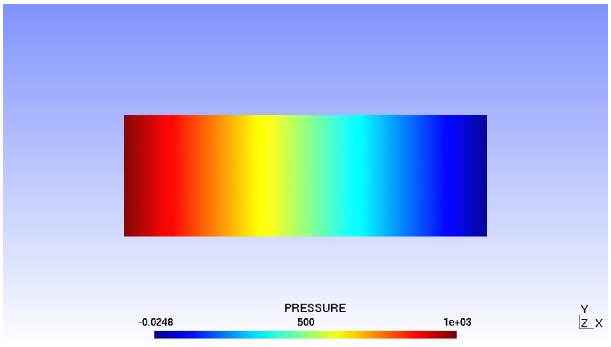

(b) pressure

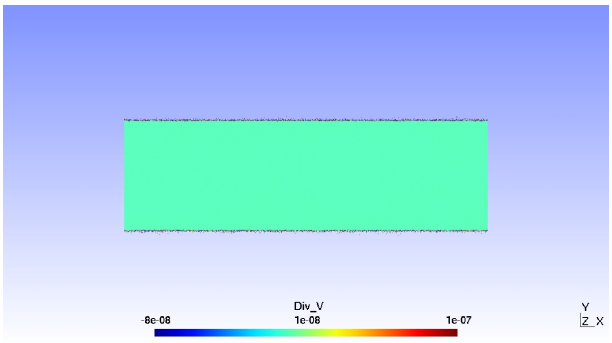

(c) velocity divergence

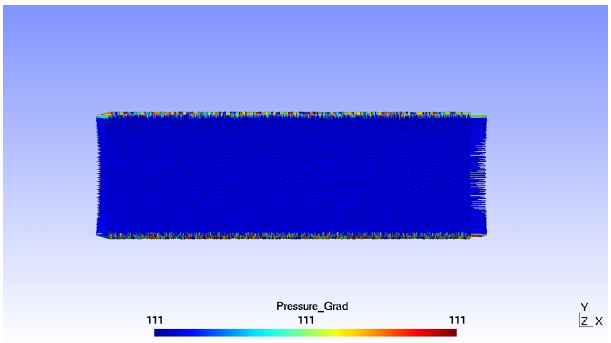

(d) pressure gradient

Figure 3.14 Results of the finer mesh test

3.2 Multi layers test

In a lot of cases, the domain are not pure material, but constructed by some layers of materials. Take the water go though the wall as a simple example, as there are always some pipes or some other things inside, the domain is no longer an easy material. Thus it could be interesting to simulate the flow through the layers of materials. In this paper, three layers of materials was tested. The index for the layer from top to the bottom is from 1 to 3. The material for the first layer is the same as that of the third layer which make the domain to be symmetric. So the simulation could be simply based on the half of the whole domain. The mesh of the half domain is shown in figure 3.15(a).

Because there are two layers of materials, if the whole domain is meshed based on the whole domain, then at the boundary of layers, even the level set method was used to distinguish the material, the level set will go though some elements at the boundary elements which will absolutely result in some discontinuous of using the properties of the materials. To avoid the error from this discontinuities, during the meshing process, the boundary of the material was built. This will make the level set used to distinguish the layers not go through any element but all though nodes. The mesh is treated as in figure 3.15(b).

There are many ways to impose the level set to distinguish the materials. For three layers, either two planes of LS could be imposed or one cylinder will work. In this case, the cylinder was imposed as: one material is inside the cylinder and the other two are outside. The origination of the imposed cylinder is at the center point at the y direction of the material, the radius is the width of the one kind of material and the normal of the cylinder is along the x direction in the test. The value of the level set is shown in figure 3.16

The boundary condition is as what has imposed before. Still the capillary pressure was considered. Thus the domain is slim. The no slip condition was imposed. The boundary condition could be described as,

- $\overrightarrow{v} \cdot \overrightarrow{e}_x = 0$ and $\overrightarrow{v} \cdot \overrightarrow{e}_y = 0$ at the bottom;
- $\overrightarrow{v} \cdot \overrightarrow{e}_x = 0$ and $\overrightarrow{v} \cdot \overrightarrow{e}_y = 0$ at the top;
- $\overrightarrow{v} \cdot \overrightarrow{e}_y = 0$ and $\boldsymbol{\sigma} \cdot \overrightarrow{n} = \overrightarrow{t} = 0Pa$ at the right side ;
- $\overrightarrow{v} \cdot \overrightarrow{e}_y = 0$ and $\boldsymbol{\sigma} \cdot \overrightarrow{n} = \overrightarrow{t} = 10000Pa$ at the left side ;

Then the problem ware solved with the first and the second degree of the interpolation.The results of first and second degree of interpolation are shown in figure 3.17 and respectively. It could be observed from figure 3.17 that the result is not so good. The biggest velocity is 33.8 occurred in the middle part of the domain and magnitude of the divergence velocity is almost 10. The pressure changes from 2.39 at the right side from 999 to the left side. And the pressure gradient varies from 19.5 to 563. However, in the boundary condition, the pressure at the left side was prescribed to be 1000 and the at the right side was prescribed to be 0 which is different with the result.

But from figure , it could be observed that the result of the second degree of the interpolation is much better. The velocity profile is almost the same with the result of the fist degree, but the magnitude of the divergence of the velocity field is 10^{-10} which is perfect. And the pressure changes from 0 at the right side to 1000 at the left side, this is consistent with the boundary condition. what is more is the gradient of the pressure is homogeneous which means the pressure changes steadily from the right to the left side.

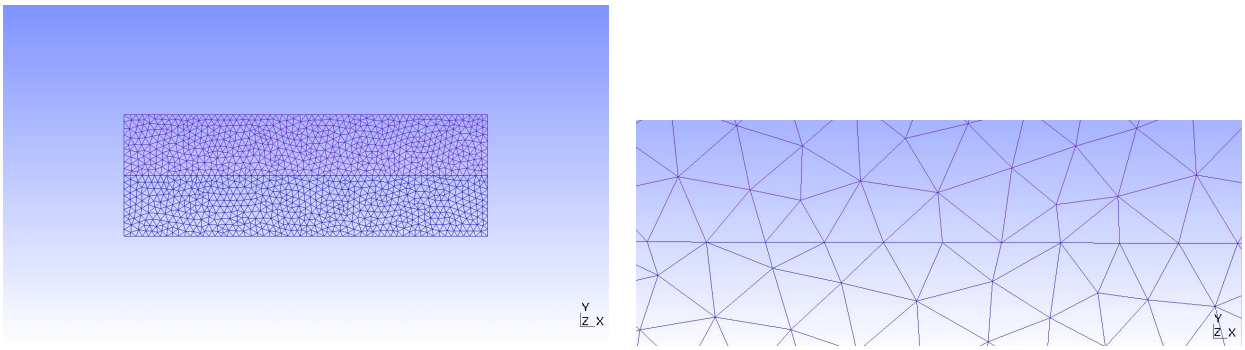

(a) The two layers of material mesh

(b) the boundary of the two layers of materials

Figure 3.15 The mesh of the two layers of materials

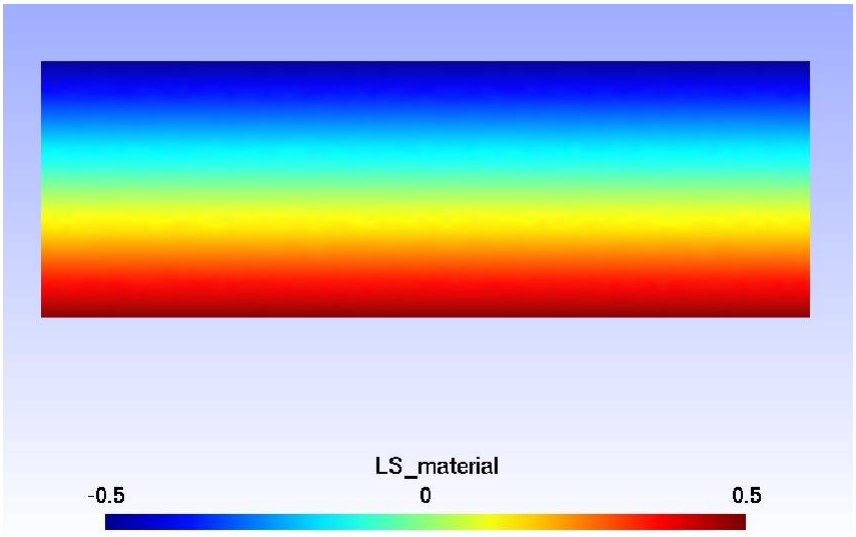

Figure 3.16 The level set of the material boundary

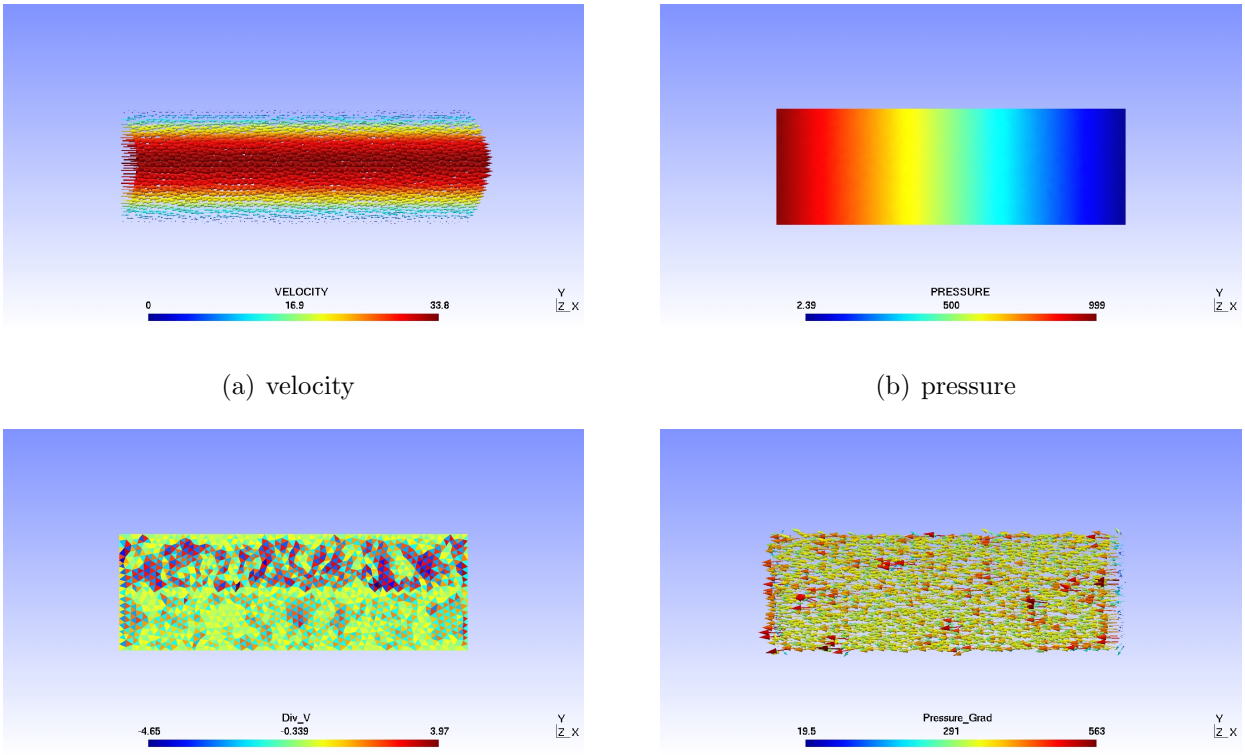

(a) velocity

(b) pressure

(c) velocity divergence

(d) pressure gradient

Figure 3.17 the composite test with the first degree of the shape function

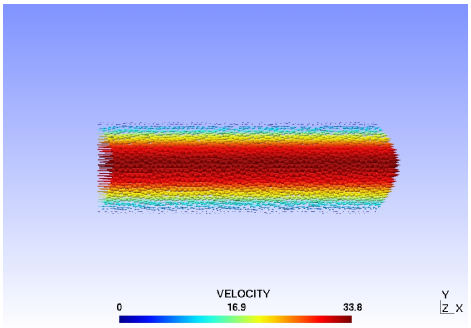

(a) velocity

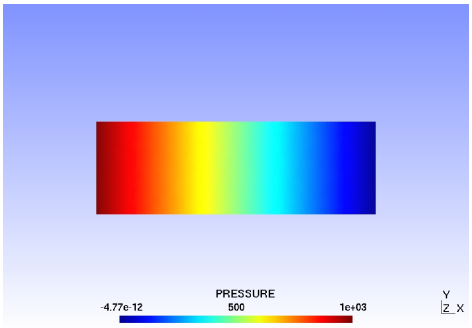

(b) pressure

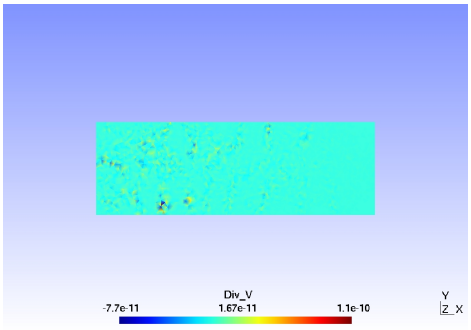

(c) velocity divergence

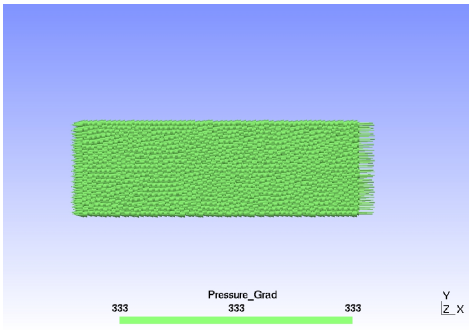

(d) pressure gradient

Figure 3.18 the composite test with the second degree of the shape function

3.3 Anisotropic test

The isotropic permeability was used in all the previous tests. However, an anisotropic permeability is characteristic of impregnation of fibrous systems and will be introduced here. We consider an orthotropic medium where the main directions are given by vectors $\overrightarrow{e}_I$, $\overrightarrow{e}_{II}$ and $\overrightarrow{e}_{III}$. In this frame the materials' permeability is assumed to be $\boldsymbol{K}_{ref}$ with

$$\boldsymbol{K}_{ref} = \begin{bmatrix} K_I & 0 & 0 \\ 0 & K_{II} & 0 \\ 0 & 0 & K_{III} \end{bmatrix} \tag{3.1}$$

where K_I, K_{II} and K_{III} are the three main values of permeability along the $\overrightarrow{e}_I$, $\overrightarrow{e}_{II}$ and $\overrightarrow{e}_{III}$.

In the physical space, the fibers are assumed to be rotated of an angle θ around $\overrightarrow{e}_{III}$ so that the permeability tensor can be expressed as $\boldsymbol{K} = \boldsymbol{R}_\theta^T \cdot \boldsymbol{K}_{ref} \cdot \boldsymbol{R}_\theta$. In this relation, $\boldsymbol{R}_\theta$ is the rotation matrix of angle θ:

$$\boldsymbol{R}_\theta = \begin{bmatrix} cos\theta & -sin\theta & 0 \\ sin\theta & cos\theta & 0 \\ 0 & 0 & 1 \end{bmatrix} \tag{3.2}$$

To test the influence of the angle of the permeability to the velocity, the boundary conditions are prescribed as:

- $\overrightarrow{v} \cdot \overrightarrow{e}_y = 0$ at the top and at the bottom;
- $\overrightarrow{v} \cdot \overrightarrow{e}_y = 0$ and $\boldsymbol{\sigma} \cdot \overrightarrow{e}_x = 0Pa$ at the right side ;
- $\overrightarrow{v} \cdot \overrightarrow{e}_y = 0$ and $\boldsymbol{\sigma} \cdot \overrightarrow{e}_x = 10000Pa$ at the left side ;

- angle of permeability $\theta = 45°$

The results were plotted in figure 3.19.

It can be observed that because of the anisotropy, the direction of the pressure gradient is no longer along x direction. And for velocity, most of the part it is homogeneous, but at the right up corner, it is much bigger than the homogeneous value, and at the right low corner, it is much smaller than the homogeneous value. The same problem for the divergence of the velocity, its magnitude is not so bad in most of the domain except the right side. Results are physically consistent, but with the same boundary conditions as in the filtration tests, results are not homogeneous anymore.

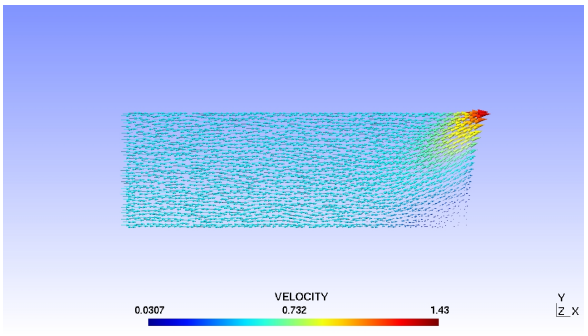

(a) velocity

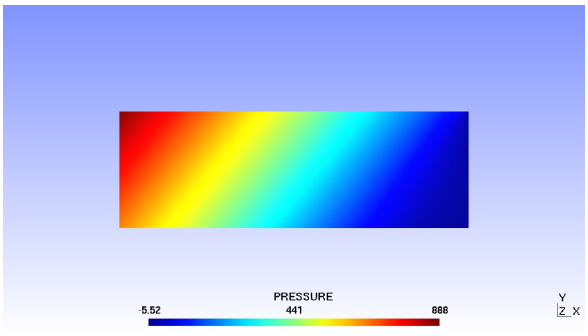

(b) pressure

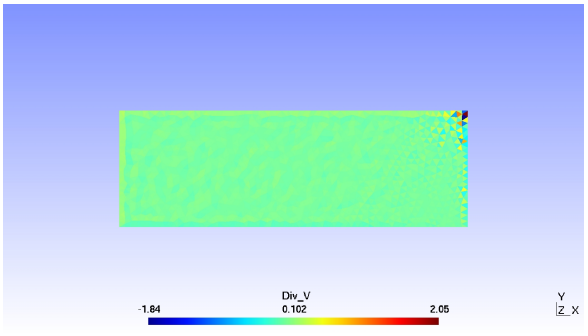

(c) velocity divergence

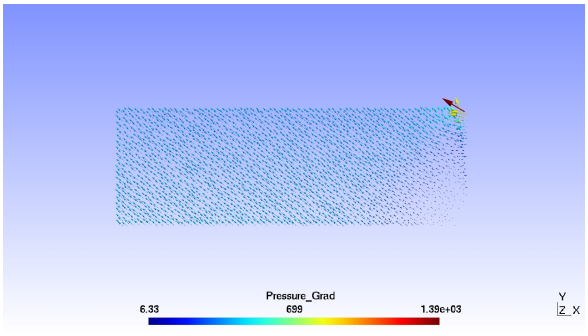

(d) pressure gradient

Figure 3.19 anisotropic test with angle of 45°

3.4 Propagation of flow front

The basic idea to investigate the propagation of the flow front is to use the level set method. After defining the flow front as a level set, the propagation behavior can be computed by solving the velocity over the whole domain. Previously, the code used to use level set to distinguish the different properties of the material like what have done for the multi layer test. However, when using this method for the flow front, the problem could be complicated. Where the whole domain is not fully filled with the flow, the property of the air has to be considered. In this way, if the level set was employed to distinguish the material, there should at least one more level set for the air. Thus, using function to tell the difference between the materials could be a better way.

For the tests, the property needed to be distinguished is the permeability. According to equation (2.25), the term $[N_v]^T c[N_v]$ in the Jacobean matrix is no longer a constant. It now depends on the geometry thus the space. So it can not be directly transfered from the property of the material to the integration process. It needed to be calculated where the information of the space could be obtained. The same for the term of $\int_\Omega c\overrightarrow{v} \cdot \overrightarrow{N}_v$ of the function $\boldsymbol{r}(\overrightarrow{v}, p)$.

The first test was set for the simple square mesh. The permeability was set to be $k = a+b*y$, where a and b are 0.01, 0.2 respectively, y is the vertical coordinate of the integration point. The permeability is exported as figure 3.20(a).

A constant pressure difference was prescribed between the upper and lower side, while a null normal velocity of 0 was imposed for the left and right sides. The initial flow front was defined as figure 3.20(b). The total time is 0.2 second and the number of the iteration is 32.

The propagation of the flow front is illustrated by figure 3.21, where the different locations of the flow front in time as plotted.

It can be observed that the flow front moves forward slower with the increase of the time which is reasonable. Because the permeability is $k = a + b * y$, depends on y, and as b is positive, the permeability decreases with the decrease of the vertical coordinate. That means the permeability of the lower part is smaller than that of the upper part. Thus the ratio of the space for the upper part is bigger than that of the lower part, so the flow front could move faster in the upper part.

In a particular forming process called "pultrusion", fibers are pulled through a cavity which is filled by a viscous polymeric liquid. In order to be able impose the fibers velocity, a volumic force $\overrightarrow{f}$ was imposed such as:

$$\overrightarrow{f} = c\,\overrightarrow{v}_{imp} \tag{3.3}$$

$\overrightarrow{v}_{imp}$ denoting the imposed fibers velocity. Then the Brinkman equation (2.6) can be rewritten as:

$$div\boldsymbol{\sigma^d} - \nabla p - c(\overrightarrow{v} - \overrightarrow{v}_{imp}) = 0 \tag{3.4}$$

By employing finite element method and imposing the test function $\overrightarrow{v}^*$ and p^*, equation (3.4) can be transformed into

$$\begin{aligned} \forall(\overrightarrow{v}^*, p^*): \quad & \int_\Omega \boldsymbol{T} : \nabla \overrightarrow{v}^* d\Omega - \int_{\partial\Omega} (\overrightarrow{t} \cdot \overrightarrow{v}^*) d\partial\Omega \\ & - \int_\Omega (p^* \cdot div\,\overrightarrow{v}) d\Omega + \int_\Omega c(\overrightarrow{v} - \overrightarrow{v}_{imp}) \cdot \overrightarrow{v}^* d\Omega = 0 \end{aligned} \tag{3.5}$$

Using the shape function $[N_v]$ and $[N_p]$ for the interpolation of $\overrightarrow{v}$ and p respectively and employing the value $\{\overrightarrow{v}^*_{node}\}$ and $\{p^*_{node}\}$ at each node for velocity and pressure, the equation

(3.5) could be rewritten

$$\begin{aligned} R(\overrightarrow{v}, p) = &\int_\Omega \boldsymbol{T} : \{\{\overrightarrow{v}^*_{node}\}\nabla[N_v]\}d\Omega - \int_{\partial\Omega} \overrightarrow{t} \cdot \{\{\overrightarrow{v}^*_{node}\}[N_v]\}d\partial\Omega \\ &- \int_\Omega \{p^*_{node}\}[N_p] \cdot div\,\overrightarrow{v}\,d\Omega + \int_\Omega c(\overrightarrow{v} - \overrightarrow{v}_{imp}) \cdot \{\{\overrightarrow{v}^*_{node}\}[N_v]\}d\Omega \\ =&0 \end{aligned} \tag{3.6}$$

Therefore, the function $\overrightarrow{r}$ to be solved is

$$\overrightarrow{r} = \begin{bmatrix} \dfrac{\partial R}{\partial\{\overrightarrow{v}^*_{node}\}} \\ \dfrac{\partial R}{\partial\{p^*_{node}\}} \end{bmatrix} = \int_\Omega \begin{bmatrix} \boldsymbol{T} : \nabla[N_v] + c(\overrightarrow{v} - \overrightarrow{v}_{imp}) \cdot [N_v] \\ -[N_p] \cdot div\,\overrightarrow{v}\,d\Omega \end{bmatrix} - \int_{\partial\Omega} \begin{bmatrix} \overrightarrow{t} \cdot [N_v] \\ 0 \end{bmatrix} = \mathbf{0} \tag{3.7}$$

The Jacobean matrix is unchanged.

By observing the equation (3.4), if the coefficient $c = \dfrac{\mu_e}{k}$ is big enough, it is expected that the velocity field will be almost the same as the field of the imposed velocity $\overrightarrow{v}_{imp}$.

A test was made to check the expectation. The boundary condition is prescribed as following: the length and the width of the domain are 6 and 2 respectively. The bottom of the domain is totally free while the top side of the domain was bounded. For the left side and the right side, the vertical velocity are zero. However, the horizontal velocity is prescribed to be 1 for both the left and right sides of the lower part while the pressure for them are zero. And for that of the upper part, the constant pressure difference of 1000 are prescribed with the direction of x positive. For both materials, consistent with the boundary condition, the volumic force is defined as $(1, 0, 0)$. The initial position of the flow front is as figure 3.22.

For the permeability, as what have done before, instead of using level set to distinguish the difference, the function was imposed to distinguish that. To describe the sharp change

between the layers of the materials, the function imposed was

$$k = 0.5 * 10 * (1 + tanh(2000 * (y - 0.5 * h))) + 1.0e - 3 \tag{3.8}$$

where h here stands for the height of the domain, it was $10mm$ for this test. Therefore, by using this function, the permeability for the upper part is about $10m^2$ while 10^{-3} for the lower part, and the permeability at the boundary of the material is continuous which is more practical than just imposing two constant for the two layers. The result is got as figure 3.26.

As it was expected before the test, at the lower part, as there is no difference of pressure, the influence of the first two terms in equation (3.4) could be negligible. Thus the result of the velocity field is almost exactly the same as the imposed volumic force. While at the upper part, $1000Pa$ of pressure difference was imposed, so the solution are influenced by both the pressure gradient and the volumic force which means the velocity would not be same as the volumic force any more. The same reason for the gradient pressure, as the imposed pressure difference is $1000Pa$ which is big enough to eliminate the influence of the volumic force on the pressure gradient, the gradient profile of the upper part is almost constant from 330 to 335, while the pressure gradient of the lower is affected mainly by the volumic force, thus it varies a lot from 335 to $1.46e + 03$.

As the imposed volumic external force was only along x direction, by recalling the equation (2.37),

$$\frac{d}{dt}\phi(\overrightarrow{x}(t), t) = \frac{\partial \phi}{\partial t} + |\overrightarrow{\nabla}\phi| v_n = 0 \tag{3.9}$$

the flow front in this test should not be moved which was proved by the figure 3.26.
The total time is 1 second and there are 100 iterations which means the time step imposed should 0.01 seconds. In figure 3.26, the position of the flow front every 10 steps from the

Table 3.2 Comparison of parameters for both materials

material	viscosity	intrinsic viscosity	volumic force
air	0.1	0.1	(1,0,0)
water	10	10	(1,0,0)

first step is given. To illustrate the flow front, the value of the level set from 0 to 0.1 was drawn. It could be seen that the position of the flow stays the same during the simulation.

To fill the whole cavity, another more practical test was done. In this test, the domain with the size of $100mm \times 10mm$ was defined which is consistent with a practical mold. It is consisted of two layers of material, the parameters defined for the material are a little bit different from the practical one. They are given in table 3.2. By checking online, the difference of the magnitude of the viscosity is 2, and the magnitude of the the viscosity and the intrinsic viscosity is the same.

The boundary condition for this test was: a symmetrical boundary condition was imposed for the bottom of the cavity, that means the flow along the x direction is free but the along the y direction should be zero. This is because the mold simulated for the test is actually half of the whole cavity. Indeed, as the whole cavity is symmetry along y direction, it is reasonable to simulate half of it. The right side of the domain was free while a constant pressure of $1000Pa$ was prescribed for the left side. The no slip boundary condition was imposed at the top of the domain.

The flow field after the first time step was obtained as figure 3.26.Firstly, it can be seen that the problem for the divergence of the velocity field is still mainly around the boundary.

The value scale for the divergence of the velocity field adjusted to be from -1 to 1 which enables the figure to display the problem for that clearly. From figure 3.26(a) and 3.26(b), the x velocity for the bottom part is obviously bigger than that of the upper part which is reasonable regarding the prescribed boundary condition; the y-velocity for the air is almost zero but highest velocity at the flow front. The pressure is almost constant for the air but got a sharp change through the flow front.

The propagation of the flow front is shown in figure 3.22. The calculation was carried out within $1.5s$. The condition to end the loop of the propagation is the time reach the maximum time. As it could seen the field was filled quite well, and the flow front at the bottom part moved faster than that of the upper part which was expected as illustrated as before.

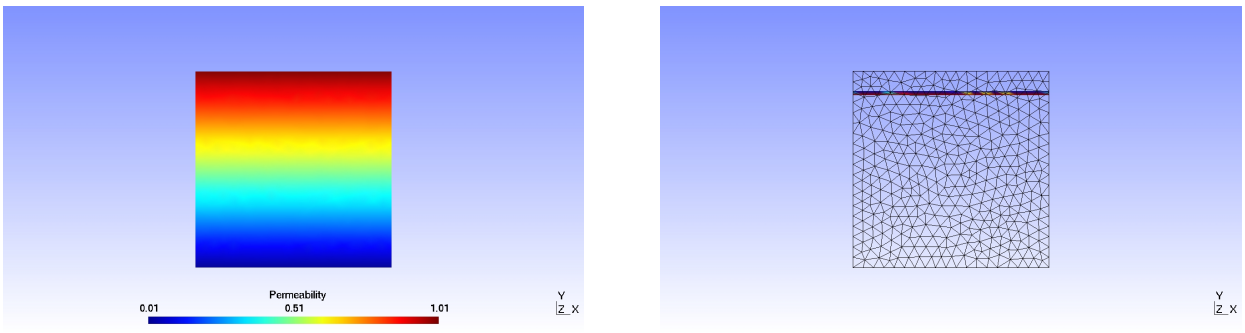

(a) permeability of the simple square mesh

(b) initial position of the flow front, first test

Figure 3.20 initial condition of the propagation test

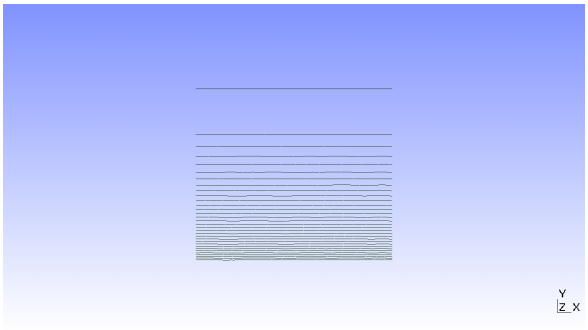

Figure 3.21 propagation of the flow front

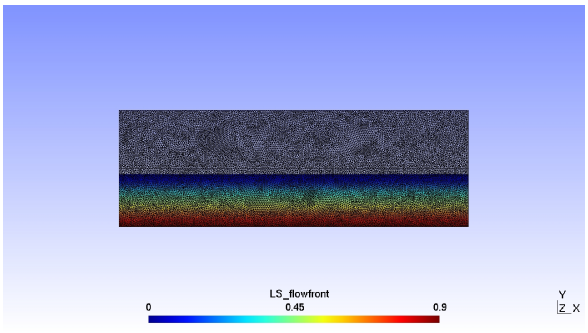

Figure 3.22 initial position of the flow front, second test

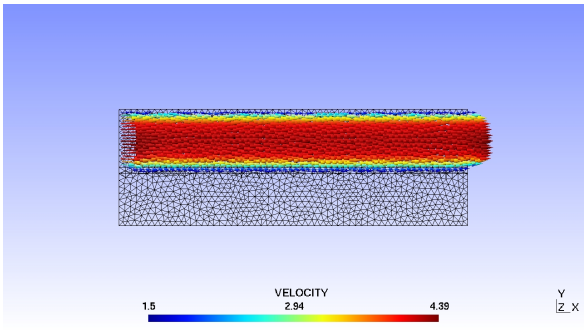

(a) velocity of the upper part

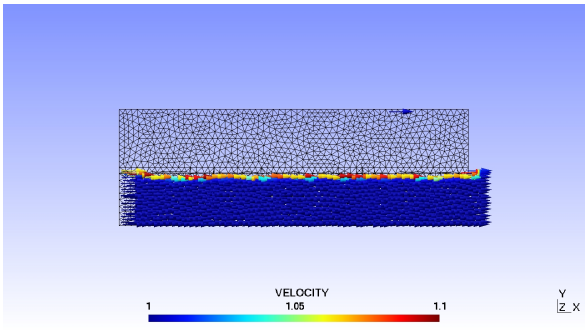

(b) velocity of the lower part

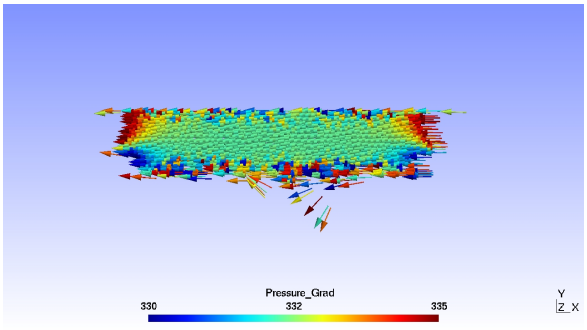

(c) pressure gradient of the upper part

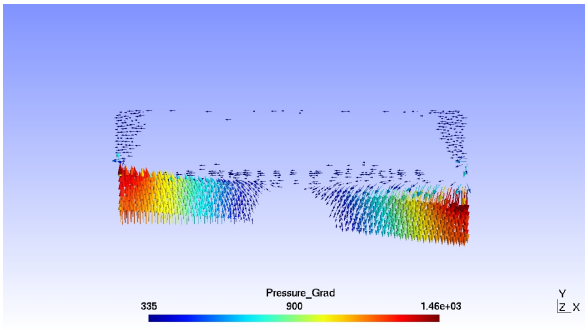

(d) pressure gradient of the lower part

Figure 3.23 Results of the body force test

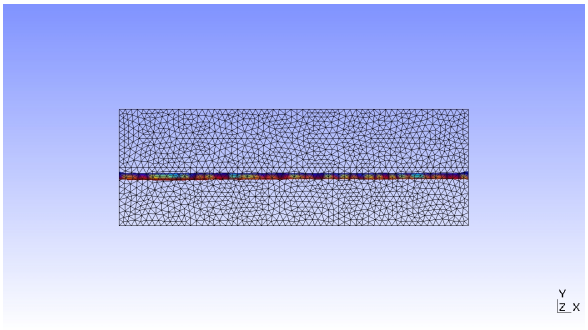

Figure 3.24 propagation of the flow front with the horizontal volumic force

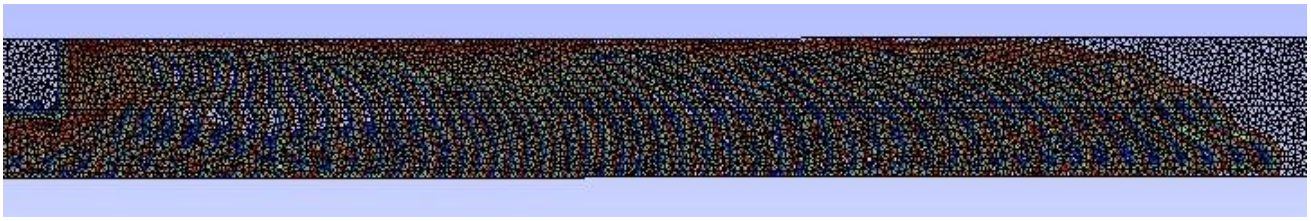

Figure 3.25 propagation of the flow front of the practical test

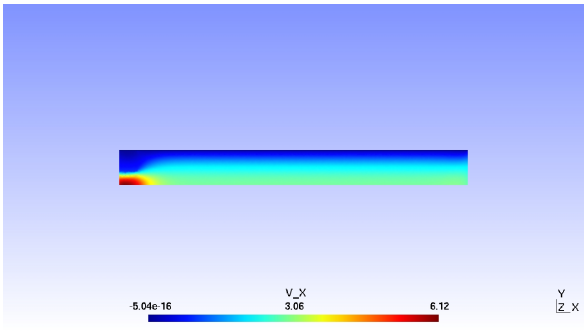

(a) x velocity profile

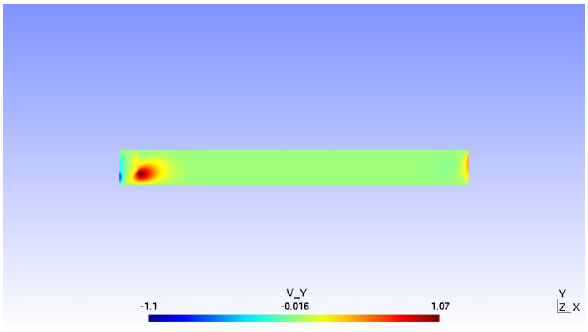

(b) y velocity profile

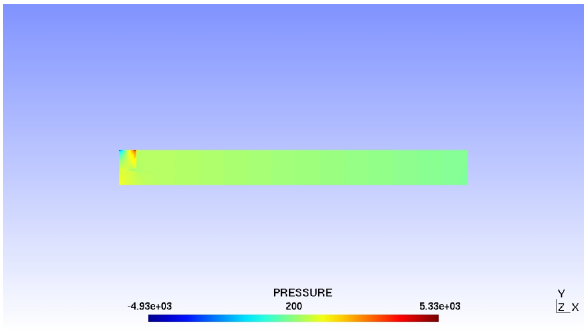

(c) pressure

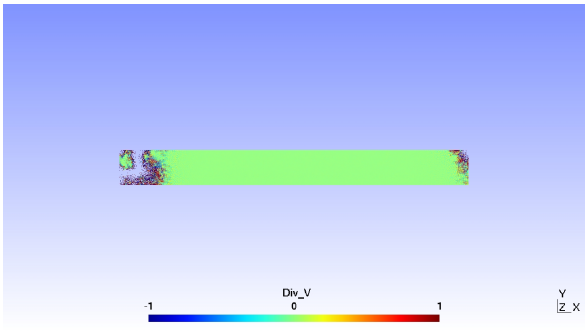

(d) velocity divergence

Figure 3.26 Results of the body force test after the first time step

Chapter 4

Conclusions and Preview

Based on the finite element method, the Stokes equation was firstly solved. Darcy's assumption was employed to simplify the equation for the flow through the porous media and led us to employ the Brinkman formulation.

Firstly, with the coefficient of the Brinkman term to be zero, the test was done to compare the result with that of Stokes. As expected the both results are consistent with each other. Then the simulation was done for the Brinkman equation with a serious of values of the Brinkman coefficient. The influence of the coefficient on the velocity at the bottom of the domain was investigated. The domain was then transfered to be a long enough square from a block to study the capillary pressure, and the influence of the capillary pressure was figured out. To get closer to reality, the same test for the 3D mesh simulation was carried out. After all these simulation above, it was found that for the 1D filtration test, the solution works perfectly with the incompressible condition satisfied everywhere. However, for the no slip condition case, the problem mainly focus near the boundary, thus the mesh was adapted much finer near the boundary while the mesh at middle of the domain was kept the same as before.

Exactly as what was expected, the results were much better since the mesh was finer near the boundary which is enough to enable the make of the conclusion that the solution is really mesh sensitive. With finer mesh on a more powerful computer, the solution could be expected to be better. Because the reality of the permeability is not isotropic, it was also interesting to study the influence of the anisotropic permeability for practical reason, which was done. And the influence of the angle of the permeability on the velocity was investigated. In the real industry, take the pipe inside the wall of the building as an example, the media in this case is no longer a single one, thus the simulation was carried out with multi layers of materials. During the study, two methods were adopted to distinguish the materials. The first one was using the level set, the algorithm of which was illustrated in the second chapter. The second one was by defining a spatially variable property. With this one, it is easy for the steady case as the boundary of the material does not change with the time and it is employed. As the tests before, the simulation works very well for the filtration test while for the no slip condition case, the mainly problem is still on the boundary.

Finally the propagation of the flow front was also implemented and investigated for the Brinkman formulation. Within this simulation, the second method to distinguish the material was adopted, using an almost sharp change function to describe the evolution of the properties change at the boundary of the material. Actually, it is more realistic, as in the real world nothing is gonna change suddenly, there should be some mixed region at the boundary with the two different materials which enables the properties of the materials to be continued. The first test was done to check the validity of this method with the homogeneous mesh used for the very first simulation while in this test, the permeability is no longer a constant, but a function of the y coordinate. The propagation of the flow front was

then simulated and it works very well. That built the confidence to go further to use this method for the multi layers of materials. To distinguish the change of the materials, the sharp change function *tanh* was then adopted. With imposing the CFL condition for the time step, the results were acceptable. However, the flow front sometimes go through some elements, so that the propagation of the curve of the flow front is sometimes not perfect.

Thus for the preview of the work, the main problem is to handle the discontinuities within the calculation. There are two basic ways to do that. The first is to simply refine the mesh. However that really has a huge requirement of the capability of the computation of the computer. The second way is to use some numerical methods to eliminate the discontinuities. There are a lot of these kinds of numerical, based on the library of the Ecole Centrale de Nantes, the XFEM will be the very perfect method to deal with the discontinuities.

Bibliography

[1] Yeonhee Jung, Wanl Byun and Seung Jo Kim, "Mathematical Modeling of Resin Transfer Molding Process: A Review"

[2] "United States Patent Kolavnnu et al. Patent No.: US 6,856,856, B1"

[3] ZHANG Kaipeng, TAN Hua, WANG Jihui and ZHU Yingdan, "Numerical Simulation of Mold Filling in Resin Transfer Molding Using Isoparametric Method"

[4] Logan, D.L., *A first course in the finite element method*, 4th ed. (Thomson, University of Wisconsin-Platteville, 2007), p. 2.

[5] Nicolas Moes, *The eXtended Finite Element Method(X-FEm)*, (Ecole Centrale de Nantes, Institute GeM, UMR CNRS 8183), p. 3

[6] Nicolas Moes et Gilles Marckmann avec les contributions de Yosra Guetari et Eric Bechet *The XFEM User Guide*, (Institut de Recherche en Genie Cinie Civil et Mecanique Ecole Central de Nantes, 2008), p. 9

[7] Osher, S.; Sethian, J. A. (1988), "Fronts propagating with curvature-dependent speed: Algorithms based on Hamilton-Jacobi formulations", J. Comput. Phys. 79: 1249.

[8] Carolyn L. Phillip, "The Level-Set Method"

[9] "Gmsh introduction", http://geuz.org/gmsh/ (Accessed Octorber, 2010)

[10] Michael Hank, "Short Introduction to Comsol Multiphysics", June 1, 2002

[11] Byoung Yoon Kim, Gi Joon Nam, Ho Sok Ryu and Jae Wook Lee, "Optimization of filling process in RTM using genetic algorithm", (Department of Chemical Engineering, Sogang University), Korea-Australia Rheology Journal Vol. 12, No. 1, March 2000 pp. 83-92

[12] H. Darcy (1856), "Les Fontaines Publiques de la Ville de Dijon", Dalmont, Paris

[13] INGRAM, R.N, "A mixed Finite Element approximation of Stokes-Brinkman and NS-Brinkman equation for Non-Darcian flows"

[14] Frederic Dupont, "Finite Element Models", September, 1, 2001

[15] Franois Dubois, Michel Salan, Stephanie Salmon, "Vorticity-velocity-pressure and stream function-vorticity formulations for the Stokes problem", Journal Mathematics, July, 2003

[16] Per-Olof Persson "Implementation of Finite Element-Based Navier-Stokes Solver 2.094-Project" April 25, 2002

[17] R. T. Haftka *EML5526 Finite Element Analysis: Isoparametric Elements*, University of Florida. 16 February 2011

[18] Liu XD, Osher S, Chan T, "Weighted Essentially Nonoscillatory Schemes", JOURNAL OF COMPUTATIONAL PHYSICS 115 (1): 200-212 NOV 1994

[19] G. R. JERAULD, S. J. SALTER "The Effects of Pore-Stucture on Hysteresis in Relative Permeability and Capillary Pressure: Pore-Level Modeling"

[20] Aalok Shah, "Hamilton-Jacobi Equations and Level Set Methods" May 15, 2009

[21] Arthur LEVY, "Modélisation et simulation d'un écoulement sous vibration. Application au soudage par ultrasons de composites à matrice thermoplastique.", 18 décembre 2009.

[22] "Newton Raphson method", http://en.wikipedia.org/wiki/Newton's_method (Accessed Octorber 20, 2010)

Appendix A

The compiling process of the Xfem library on the personal computer

The needed libraries for the right simulation include: MeshMachine, Solver, SoverInterfaces, Trellis, Util, Xfem, Xext. After using the SVN to check all the necessary libraries to computer. The next step is to compile all of them. As not all the libraries are needed, only few of them need to be compiled. The compiling order is as following:

- SolverInterfaces/SolverBase
- SoverInterfaces/SuperLU
- MeshMachine / LinearAlgbra
- SoverInterfaces/Mtl
- Xfem
- Xext
- Physics

- SolverInterfaces/NonLinearSolver
- SolverInterfaces/Itl
- install the gfortran library
- install the libblas and the liblapck libraries

After this compiling process, the application of the simulation could be compiled successfully.